Global stability and parameter analysis reinforce therapeutic targets of PD-L1-PD-1 and MDSCs for glioblastoma

Hannah G. Anderson[1], Gregory P. Takacs[3], Duane C. Harris[2], Yang Kuang[2], Jeffrey K. Harrison[3] and Tracy L. Stepien[1*]

[1]Department of Mathematics, University of Florida, Gainesville, FL, USA.
[2]School of Mathematical and Statistical Sciences, Arizona State University, Tempe, AZ, USA.
[3]Department of Pharmacology and Therapeutics, University of Florida, Gainesville, FL, USA.

*Corresponding author(s). E-mail(s): tstepien@ufl.edu;
Contributing authors: hannahanderson@ufl.edu; gtakacs@ufl.edu; dharri31@asu.edu; kuang@asu.edu; jharriso@ufl.edu;

Abstract

Glioblastoma (GBM) is an aggressive primary brain cancer that currently has minimally effective treatments. Like other cancers, immunosuppression by the PD-L1-PD-1 immune checkpoint complex is a prominent axis by which glioma cells evade the immune system. Myeloid-derived suppressor cells (MDSCs), which are recruited to the glioma microenviroment, also contribute to the immunosuppressed GBM microenvironment by suppressing T cell functions. In this paper, we propose a GBM-specific tumor-immune ordinary differential equations model of glioma cells, T cells, and MDSCs to provide theoretical insights into the interactions between these cells. Equilibrium and stability analysis indicates that there are unique tumorous and tumor-free equilibria which are locally stable under certain conditions. Further, the tumor-free equilibrium is globally stable when T cell activation and the tumor kill rate by T cells overcome tumor growth, T cell inhibition by PD-L1-PD-1 and MDSCs, and the T cell death rate. We use the Approximate

Bayesian Computation (ABC) rejection method to construct probability density distributions that estimate model parameters with a set of preclinical experimental data. These distributions inform an appropriate search curve for global sensitivity analysis using the extended Fourier Amplitude Sensitivity Test (eFAST). Sensitivity results combined with the ABC method suggest that parameter interaction is occurring between the drivers of tumor burden, which are the tumor growth rate and carrying capacity as well as the tumor kill rate by T cells, and the the two modeled forms of immunosuppression, PD-L1-PD-1 immune checkpoint and MDSC suppression of T cells. Additionally, numerical simulations along with ABC results suggest that the activated T cell population could be maximized by targeting the immune suppression by the PD-L1-PD1 complex and MDSCs. Thus, treatment with an immune checkpoint inhibitor in combination with a therapeutic targeting MDSCs, such as a CCR2 antagonist, should be explored.

Keywords: immune checkpoint; immunosuppression; mathematical oncology; approximate Bayesian computation; sensitivity analysis

MSC Classification: 92C50 , 92-10 , 92-08 , 92-05 , 34A12 , 34D20

1 Introduction

Glioblastoma (GBM) is the most common type of primary brain cancer, claiming tens of thousands of lives each year. Within 5 years of diagnosis, less than 10% of GBM patients survive, and most succumb to the tumor within 15 months of diagnosis—even with treatment (Ostrum et al (2015); Fernandes et al (2017)). The current standard of care for this highly aggressive brain tumor includes surgical resection followed by radiotherapy and chemotherapy with temozolomide (TMZ) (Stupp et al (2005); Fernandes et al (2017)), but the minimally effective results demonstrate a need to look for new treatment strategies. A major difficulty in treating GBM is its highly complex and immune suppressed tumor microenvironment, thus immunotherapy, which has shown to be effective in some cancer types, holds promise (Brown et al (2018)).

In the last decade, an increasing number of immunotherapies have been developed for GBM (Yu and Quail (2021); Bausart et al (2022); Bryukhovetskiy (2022)). Anti-PD-1 is a standard immunotherapy that has proven to be beneficial in treating other cancers, such melanoma (Postow et al (2015)), Hodgkin's lymphoma (Ansell et al (2015)), colon (Duraiswamy et al (2013)), cervical (Ros et al (2019)), and non-small cell lung cancer (NSCLC) (Brahmer et al (2015)), although it has failed as a monotherapy in GBM phase III clinical trials (Preusser et al (2015b); Reardon et al (2017); Lim et al (2018)). One way that cancer evades the immune system is by expressing the marker PD-L1, which downregulates the cytotoxic response of activated T cells by binding to their PD-1 receptor. Treatment with anti-PD-1 unmasks the tumor's disguise

by binding to PD-1 on the tumor cells, thus allowing tumor recognition by T cells and an enhanced immune response. One possible explanation for the failure of anti-PD-1 monotherapy in GBM is additional mechanisms of immune suppression, i.e., infiltration of myeloid-derived suppressor cells (MDSCs), which are cells that suppress T cell activity.

Gliomas mediate recruitment of $CCR2^+$ MDSCs by releasing chemokines such as CCL2 and CCL7, which are cognate ligands of the CCR2 receptor expressed by MDSCs (Takacs et al (2021, 2022)). Higher expression of CCL2 and CCL7, as well as CCR2, within the tumor microenvironment all correlate with a worse prognosis for gliomas (Korbecki et al (2020); Chang et al (2016)). Once the MDSCs enter the tumor microenvironment, they suppress T cells through a variety of mechanisms including, but not limited to, inducing apoptosis in activated T cells (Saio et al (2001)), producing enzymes (such as arginase) which metabolize amino acids needed for T cell proliferation (Condamine and Gabrilovich (2011)), and secreting other factors which modulate the immune response (NO, TGF-β, TNF-α, H_2O_2) (Monu and Frey (2012); Markowitz et al (2017)). These mechanisms, along with MDSC promotion of angiogenesis (Vetsika et al (2019)), lead to rapid tumor progression. Treating with a CCR2 antagonist aids the immune response by reducing MDSC recruitment and thus sequestering the MDSC population to the bone marrow. Flores-Toro et al (2020) reported improved survival of two murine glioma models (KR158 and 005 GSC) with combination treatment of a CCR2 antagonist (CCX872) and anti-PD-1.

Although MDSCs seem to play a significant role in glioma progression, there are few published mathematical models of tumor–immune dynamics that incorporate these cells. Allahverdy et al (2019) presents a discrete agent-based model of MDSCs in the context of a general tumor and simulates treatment with the chemotherapeutic agent 5-fluorouracil (5-FU). Similar to Allahverdy et al (2019), the ODE model of Shariatpanahi et al (2018) for a general tumor also simulates treatment with 5-FU. Further, they include treatment with L-arginase since the model considers production of arginase I as the primary mechanism by which MDSCs suppress T cells. Liao et al (2014) highlights a mechanism of MDSC recruitment by developing a PDE model which focuses on the role of interleukin-35 (IL-35) in MDSC recruitment and tumor growth. Lai et al (2018) used a PDE model of breast cancer to determine the influence of the immune checkpoint inhibitor, anti-CTLA-4, on M2 macrophages within the tumor site. Although they did not specifically model MDSCs, their work implied that these conclusions apply to MDSCs since a subset of monocytic MDSCs differentiate into M2 macrophages. Each of these models provide a foundation for extension to incorporate the PD-L1-PD-1 immune checkpoint. Furthermore, we aim to develop a model specifically for GBM instead of a general tumor.

Mathematical models of tumor–immune dynamics range from modeling general tumors (Lai and Friedman (2017); Nikolopoulou et al (2018); Eftimie et al (2011); Mahlbacher et al (2019); Shi et al (2021); Radunskaya et al (2018);

Khyat and Jang (2022)) to specific cancers including GBM, non-small lung cancer (NSCLC), melanoma, and breast cancer (Storey et al (2020); Yu and Jang (2019); Butner et al (2021); Lai et al (2018); Banerjee et al (2015); Özköse et al (2022); Mirzaei et al (2021); Khajanchi and Banerjee (2017); Khajanchi (2021); Jafarnejad et al (2019); Perlstein et al (2019); Bitsouni and Tsilidis (2022)). Similar to Lai et al (2018), Yu and Jang (2019) also modelled the CTLA-4 immune checkpoint and included anti-CTLA-4 therapy, but restricted their focus to a four equation ODE model of tumor cells, $CD4^+$ T cells, IFN-γ, and CTLA-4. Two years earlier, Lai and Friedman (2017) modelled a different immune checkpoint, the PD-L1-PD-1 complex, by developing a PDE model of a general tumor which included other cells and molecules like dendritic cells, $CD4^+/CD8^+$ T cells, IL-2, and IL-12. Their model was used to simulate treatment with anti-PD-1 and a cancer vaccine, GVAX. This work was later reduced to an ODE model by Nikolopoulou et al (2018) which focused on tumor and T cells with intermittent and continuous anti-PD-1 treatment. Shi et al (2021) and Nikolopoulou et al (2021) extended this work by establishing the global dynamics of the model and a generalized version of the model. Storey et al (2020) applied these models to GBM by estimating parameters from in vivo murine experimental data. Their ODE model divided the immune compartment into the categories of innate and adaptive immune cells and modeled treatment with anti-PD-1 and an oncolytic viral therapy. Radunskaya et al (2018) deviated from modeling the typical immune checkpoint inhibitor, anti-PD-1, by considering treatment with anti-PD-L1 in their model of general tumor-immune dynamics, which compartmentalized interactions to be within the spleen, blood, and tumor site. While each of these previous papers focused on a specific immune checkpoint, Butner et al (2021) developed an ODE model which was not necessarily specific to the type of immune checkpoint or the type of tumor. Using this model along with patient data, Butner et al (2021) predicted the long-term tumor burden for a variety of patients being treated with different immune checkpoint inhibitors.

We develop a GBM-specific ODE model of cancer and T cell interactions that incorporates the PD-L1-PD-1 immune checkpoint along with tumor recruitment of MDSCs. Parameter values are estimated from the literature and via comparison with experimental in vivo murine data.

Our paper unfolds as follows: in Section 2, we describe the GBM-immune dynamics model along with the experimental data collection. In Section 3, we perform equilibrium and solution analysis, which is followed by parameter analysis implementing the Approximate Bayesian Computation (ABC) method used in conjunction with the extended Fourier Amplitude Sensitivity Test (eFAST) in Section 4. Numerical simulations are also provided. In Section 5, we conclude with a discussion of our results and future directions.

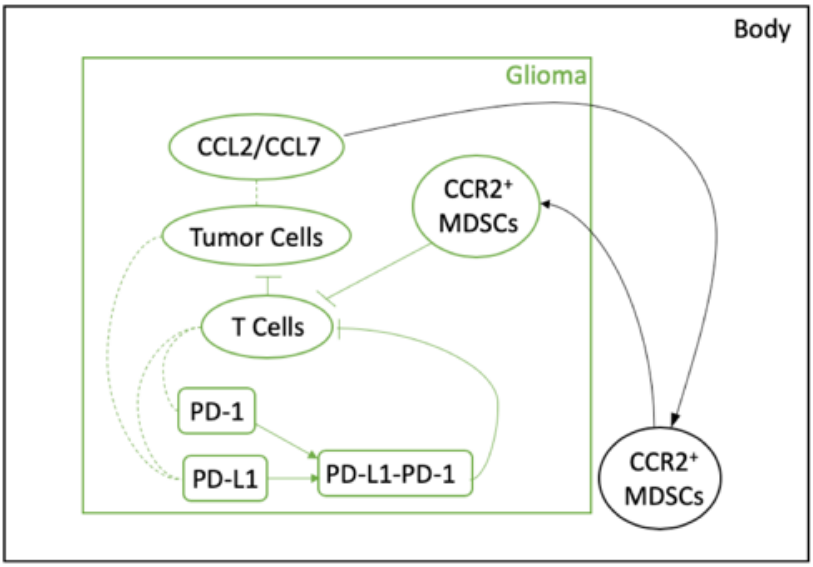

Fig. 1: A flowchart of the tumor-immune interactions in glioblastoma. The dashed lines represent proteins on the T cells or tumor cells. Sharp arrows indicate movement or recruitment. Blocked arrows indicate killing/blocking.

2 Mathematical Model

The glioblastoma (GBM)–immune model focuses on the dynamics within the glioma microenvironment, where C is the number of tumor cells, T is the number of activated T cells, and M is the number of myeloid-derived suppressor cells (MDSCs). We assume that T cells are represented by all cells that have the $CD3^+$ marker, thus including both $CD4^+$ and $CD8^+$ T cell subsets. While this model takes inspiration from Nikolopoulou et al (2018) and Storey et al (2020) in the method by which to model the PD-L1-PD-1 immune checkpoint, it is unique in that it layers this with the impact of MDSCs on glioma. We modeled MDSCs similarly to the splenic MDSCs modeled in Shariatpanahi et al (2018), yet we make this equation specific to MDSCs within the glioma through the use of experimental data and the inclusion of MDSC recruitment by the chemokines, CCL2 and CCL7. Fig. 1 illustrates a visual representation of the biological mechanisms expressed in the following equations:

$$\frac{dC}{dt} = \underbrace{\lambda_C C \left(1 - \frac{C}{C_{\max}}\right)}_{\substack{\text{logistic}\\ \text{growth}}} - \underbrace{\eta T C}_{\substack{\text{killed by}\\ \text{T cells}}}, \tag{1a}$$

$$\frac{dT}{dt} = \Big(\underbrace{a_T}_{\text{activation}} + \underbrace{s_T T C}_{\text{stimulation}} \Big) \underbrace{\frac{1}{1+\rho T(T+\epsilon_C C)}}_{\substack{\text{inhibition by}\\ \text{PD-1-PD-L1}}} - \underbrace{rTM}_{\substack{\text{inhibition}\\ \text{by MDSCs}}} - \underbrace{d_T T}_{\text{death}}, \tag{1b}$$

$$\frac{dM}{dt} = \underbrace{s_M C}_{\substack{\text{stimulation by}\\ \text{CCL2/CCL7}}} + \underbrace{\alpha \frac{C}{q+C}}_{\substack{\text{expansion}\\ \text{of MDSCs}}} - \underbrace{d_M M}_{\text{death}}. \tag{1c}$$

See Table 1 for the biological meaning of the model's 13 parameters, along with their units and range of values.

In equation (1a), we assume the tumor cells exhibit logistic growth with a carrying capacity of $C_{\max}$. T cells, which are the main drivers of tumor cell death, kill glioma cells at a rate of η. We assume that as T cells are inactivated by MDSCs, the reduction in the number of activated T cells sufficiently accounts for the reduction in the amount of T cell killing of tumor cells, i.e. the rate at which an individual T cell kills tumor cells is not reduced even as T cells are suppressed by MDSCs.

In equation (1b), activated T cells are modelled similarly to the tumor-immune models of Lai and Friedman (2017), Nikolopoulou et al (2018) and Storey et al (2020). T cells are activated at a rate of a_T, potentially due to the cytokine IL-12. The presence of a glioma results in the recruitment (or stimulation) of T cells to the tumor microenvironment.

Once in the glioma microenvironment, T cells are exhausted by the formation of the PD-L1-PD-1 complex, which forms due to interaction between PD-L1 present on glioma cells and T cells and PD-1 on T cells. Assuming $T+\epsilon_C C$ represents the level of free PD-L1 in the tumor microenvironment, the PD-L1-PD-1 complex is represented by $T(T+\epsilon_C C)$ since only T cells express PD-1. ρ represents the inhibition of T cells by the formation of the PD-L1-PD-1 complex. This parameter results from a combination of multiple parameters appearing in Lai and Friedman (2017), Nikolopoulou et al (2018) and Storey et al (2020) due to their structural non-identifiability. As T cells and tumor cells increase, more PD-L1-PD-1 complexes form, thus decreasing the overall fraction to represent T cell inhibition.

We assume T cells are suppressed/deactivated by MDSCs (Gabrilovich and Nagaraj (2009)) by a rate of r. Lastly, T cells die at a rate of d_T.

In equation (1c), we assume that gliomas recruit MDSCs to the microenvironment by secreting the chemokines CCL2 and CCL7, which are ligands for the CCR2 receptor expressed by MDSCs. This results in a chemotaxic effect drawing MDSCs from the bone marrow to the glioma microenvironment, where here we are specifically focusing on monocytic M-MDSCs as opposed to granulocytic PMN-MDSCs. Since these chemokines are produced by glioma cells, this recruitment increases as glioma cells increase. We assume that the presence of a tumor also results in the expansion of splenic MDSCs, using the same fractional term as the model of Shariatpanahi et al (2018), thus indirectly causing more MDSCs to accumulate in the tumor microenviroment. The

Table 1: Model parameters of the glioblastoma (GBM)–immune dynamics model (1). Further details on how some of these parameters were estimated are given in the Supplementary Information.

Glioma Cells			
λ_C	tumor cell growth rate	0.014–0.45 day^{-1}	Stensjøen et al (2015), Doblas et al (2010), Rutter et al (2017)
$C_{\max}$	carrying capacity of tumor cells	4.057×10^6–4.14×10^7 cell	data (see Supplementary Information)
η	kill rate of tumor cells by T cells	1.1×10^{-7} day^{-1} cell^{-1}	Shariatpanahi et al (2018), Kuznetsov et al (1994)
T Cells			
a_T	activation rate	5.25×10^2–1.18×10^6 cell day^{-1}	Lai and Friedman (2017), Nikolopoulou et al (2018), Grover et al (2011), data (see Supplementary Information)
s_T	rate of tumor cell-mediated proliferation of T cells	1×10^5–10^7 day^{-1} cell^{-1}	estimated (see Section 4.1)
ρ	inhibition of T cells by formation of PD-L1-PD-1 complex	4.17×10^{-13}–3.09×10^{-5} cell^{-2}	Nikolopoulou et al (2018), Grover et al (2011), data (see Supplementary Information)
ϵ_C	expression of PD-L1 in tumor cells vs. T cells	1–50	Storey et al (2020)
r	suppression rate of T cell proliferation by MDSCs	1×10^{-7}–5×10^{-5} day^{-1} cell^{-1}	estimated (see Section 4.1)
d_T	death rate of T cells	0.010–0.303 day^{-1}	Ribeiro et al (2002)
Myeloid-Derived Suppressor Cells (MDSCs)			
s_M	stimulation by chemokines CCL2 and/or CCL7	0.0123–0.0144 day^{-1}	data (see Supplementary Information)
α	MDSC expansion coefficient	1.6×10^7–1.2×10^8 cell day^{-1}	Cao et al (2016), Srivastava et al (2012)
q	steepness coefficient of the MDSCs production curve	10^{10} cell	Shariatpanahi et al (2018)
d_M	death rate of MDSCs	0.19 day^{-1}	Pillay et al (2010)

maximum rate of MDSC expansion is represented by α, and q represents the number of cancer cells present when this increased splenic MDSC production rate is $\alpha/2$. Lastly, MDSCs die at a rate of d_M.

2.1 Experimental Data

The mathematical model of GBM–immune dynamics developed in this study is applied to a set of experimental data obtained in the immune checkpoint inhibitor resistant high grade murine glioma, KR158.

Mice were anesthetized and surgically implanted with 35,000 glioma cells through an incision in the skull. At several time points (7, 13, 20, 24, 27, and 34 days after glioma cell implantation), 1–4 mice were euthanized followed by resection of the brain. 2D images of the glioma tissue were used to determine tumor, T cell, and MDSC cell counts (see Fig. 2).

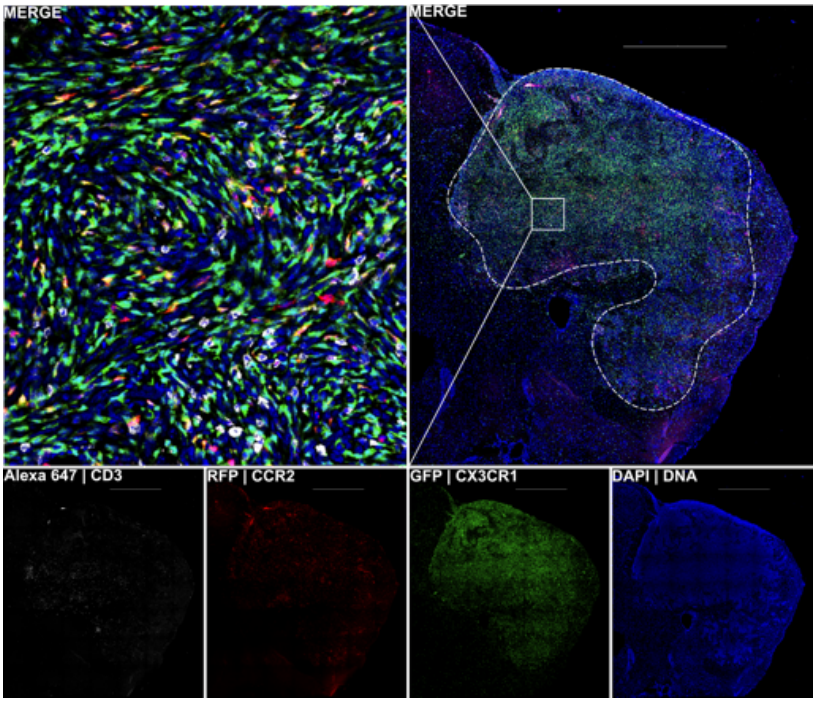

Fig. 2: Fluorescent images of brain tissue in a glioma-bearing mouse. CD3 is a marker for T cells, while MDSCs are identified by the CCR2 and CXC3R1 markers. The white, red, and green fluorescent labels denote $CD3^+$, $CCR2^+$, and $CX3CR1^+$ cells, respectively, while the blue fluorescent label denotes all viable cells. The bottom four images are overlaid in the top right image, which is then magnified (top left). A dotted white line marks the glioma's location. Notice that MDSCs are largely absent from surrounding normal brain tissue.

For a more detailed description of the experimental setup and image analysis pipeline, see Appendix A. Information on data conversion from a 2D section to a 3D spherical tumor can be found in Appendix B.

3 Equilibrium and Solution Analysis

We aim to describe the equilibria and local stability of system (1) in this section. Since the functions on the right hand side of the equations in system (1) are continuously differentiable, solutions exist and are unique by standard ordinary differential equations theory.

First, we show that solutions with positive initial conditions remain positive for all time.

Theorem 1 (Positivity) *Solutions of* (1) *that start positive remain positive.*

Proof Assume $C(t_0) \geq 0$, $T(t_0) \geq 0$, and $M(t_0) \geq 0$ for some initial time t_0. Without loss of generality, assume $t_0 = 0$.

In order to have $T(t) < 0$ for some $t > 0$, it is necessary to have $dT/dt < 0$ for $T = 0$. However, when $T = 0$, (1b) becomes

$$\frac{dT}{dt} = a_T > 0.$$

Thus, $T(t) \geq 0$ for all $t > 0$.

Assuming that C and T exist on some interval $[0, t)$ for $t > 0$, when we integrate (1a), we arrive at

$$C(t) = C(0) \exp\left(\int_0^t \lambda_C \left(1 - \frac{C(s)}{C_{\max}}\right) - \eta T(s) ds\right), \tag{2}$$

which is always positive since $C(0) > 0$.

Lastly, when $M = 0$, (1c) becomes

$$\frac{dM}{dt} = s_M C + \alpha \frac{C}{q + C}. \tag{3}$$

Since we proved that $C(0) \geq 0$ implies $C(t) \geq 0$ for all $t > 0$ and because all of the parameters are positive, we conclude that for $M = 0$, $dM/dt > 0$. Thus, $M(t) \geq 0$ for all $t > 0$. □

Next we show that solutions of system (1) with positive initial conditions are bounded.

Theorem 2 (Boundedness) *Solutions of* (1) *that start positive are bounded.*

Proof Assume $C(t_0) \geq 0$, $T(t_0) \geq 0$, and $M(t_0) \geq 0$ for some initial time t_0. Without loss of generality, assume $t_0 = 0$.

Since all parameters are positive and C and T are nonnegative by Theorem 1, by comparison we can bound (1a) by

$$\frac{dC}{dt} \leq \lambda_C C \left(1 - \frac{C}{C_{\max}}\right). \tag{4}$$

Since logistic growth is bounded, $C(t)$ is bounded as well. Specifically,

$$C(t) \leq \widehat{C} := \max\{C(0), C_{\max}\} \tag{5}$$

for all $t \geq 0$.

For the T cells, note that (1b) can be bounded as

$$\frac{dT}{dt} \leq \frac{a_T + s_T T\widehat{C}}{1 + \rho T^2} - d_T T. \tag{6}$$

Define

$$g(T) := \frac{a_T + s_T T\widehat{C}}{1 + \rho T^2}, \tag{7}$$

which achieves an absolute maximum at

$$T_m = \frac{\sqrt{\rho\left(\rho a_T^2 + (s_T\widehat{C})^2\right)}}{\rho s_T \widehat{C}} - \frac{a_T}{s_T\widehat{C}}. \tag{8}$$

Hence, (6) can be further bounded as

$$\frac{dT}{dt} \leq g(T_m) - d_T T. \tag{9}$$

Using a standard comparison argument,

$$\limsup_{t\to\infty} T(t) \leq \frac{g(T_m)}{d_T}. \tag{10}$$

Thus, for all $t \geq 0$,

$$T(t) \leq \max\left\{T(0), \frac{g(T_m)}{d_T}\right\}. \tag{11}$$

For the MDSCs, since C is bounded (5),(1c) can be bounded as

$$\frac{dM}{dt} \leq s_M C + \alpha - d_M M \leq s_M \widehat{C} + \alpha - d_M M. \tag{12}$$

By a standard comparison argument,

$$\limsup_{t\to\infty} M(t) \leq \frac{s_M\widehat{C} + \alpha}{d_M}. \tag{13}$$

Therefore, for all $t \geq 0$,

$$M(t) \leq \max\left\{M(0), \frac{s_M\widehat{C} + \alpha}{d_M}\right\}. \tag{14}$$

Hence, system (1) is bounded. □

The system (1) admits two categories of fixed points: tumor-free equilibria of the form $(C, T, M) = (0, T_0^*, M_0^*)$ and tumorous equilibria of the form $(C, T, M) = (C^*, T^*, M^*)$. We first show that there exists one unique tumor-free equilibrium.

Theorem 3 (Uniqueness of tumor-free equilibrium) *The system* (1) *has a unique tumor-free equilibrium* $(C, T, M) = (0, T_0^*, 0)$*, where* T_0^* *is increasing with respect to* a_T *and decreasing with respect to* d_T *and* ρ*.*

Proof Assume that there is no tumor present, i.e., $C = 0$. Setting $dM/dt = 0$ in (1c) implies that $M_0^* = 0$.

When $dT/dt = 0$, (1b) implies that

$$d_T T_0^* (1 + \rho {T_0^*}^2) = a_T. \tag{15}$$

Let $f(T) = d_T \rho T^3 + d_T T - a_T$. According to Descartes' rule of signs, the number of sign changes in front of the coefficients of a polynomial corresponds to the number of positive zeros. Since there is exactly one sign change because all of the parameters are positive, there is exactly one positive zero, T_0^*. Thus, a biologically relevant tumor-free equilibrium $(0, T_0^*, 0)$ exists and is unique.

Note that as a_T increases, the graph of $f(T)$ shifts down resulting in a larger T_0^*. As d_T and ρ increase, $f'(T) = 2d_T \rho T^2 + d_T$ increases for $T > 0$, which results in a narrowed curve and thus a smaller T_0^*.

Lastly, when we solve for T_0^* using the cubic formula, we obtain

$$T_0^* = \sqrt[3]{\left(\frac{a_T}{2d_T\rho}\right) + \sqrt{\left(\frac{a_T}{2d_T\rho}\right)^2 + \left(\frac{1}{3\rho}\right)^3}} + \sqrt[3]{\left(\frac{a_T}{2d_T\rho}\right) - \sqrt{\left(\frac{a_T}{2d_T\rho}\right)^2 + \left(\frac{1}{3\rho}\right)^3}}. \tag{16}$$

□

Next, we determine conditions for the stability of the tumor-free equilibrium $(0, T_0^*, 0)$.

Theorem 4 (Stability of tumor-free equilibrium) *When* $\lambda_C < \eta T_0^*$*, the tumor-free equilibrium,* $(0, T_0^*, 0)$*, is locally asymptotically stable. However, when* $\lambda_C > \eta T_0^*$*,* $(0, T_0^*, 0)$ *is a saddle point.*

Proof The Jacobian evaluated at the tumor-free equilibrium is

$$J(0, T_0^*, 0) = \begin{pmatrix} \lambda_C - \eta T_0^* & 0 & 0 \\ \frac{-a_T \epsilon_C \rho T_0^*}{(1+\rho {T_0^*}^2)^2} + \frac{s_T T_0^*}{1+\rho T_0^*} & \frac{-2a_T \rho T_0^*}{(1+\rho {T_0^*}^2)^2} - d_T & -rT_0^* \\ s_M + \frac{\alpha}{q} & 0 & -d_M \end{pmatrix}, \tag{17}$$

and the eigenvalues are

$$\lambda_1 = \lambda_C - \eta T_0^*, \tag{18a}$$

$$\lambda_2 = \frac{-2a_T \rho T_0^*}{(1 + \rho {T_0^*}^2)^2} - d_T < 0, \tag{18b}$$

$$\lambda_3 = -d_M < 0. \tag{18c}$$

Therefore, when $\lambda_C < \eta T_0^*$, the tumor-free equilibrium $(0, T_0^*, 0)$ is locally asymptotically stable. However, when $\lambda_C > \eta T_0^*$, $\lambda_1 > 0$, so the tumor-free equilibrium is a saddle point. □

Biologically, the condition $\lambda_C < \eta T_0^*$ indicates that T cells kill cancer cells faster than the cancer cells can multiply during the onset of tumor initiation, which is a reasonable expectation to guarantee the local stability of the tumor-free equilibrium.

To establish conditions under which the tumorous equilibrium exists and is unique, as well as its stability, for simplicity, we modify the equation for the tumor cells (1a) and assume that growth is exponential, i.e.

$$\frac{dC}{dt} = (\lambda_C - \eta T)C. \tag{19}$$

See the Supplementary Information for conditions required for the full model (1) with logistic growth.

Theorem 5 (Uniqueness) *The system* (1b)–(1c), (19) *has a tumorous equilibrium when* $a_T > \frac{d_T \lambda_C}{\eta}\left(1 + \rho(\frac{\lambda_C}{\eta})^2\right)$. *Further, it is unique when*

$$s_T d_M < \max\left\{s_M r, \rho\epsilon_C \alpha r\left(\frac{\lambda_C}{\eta}\right), \rho\epsilon_C d_T d_M\left(\frac{\lambda_C}{\eta}\right), s_M r \rho\epsilon_C q\left(\frac{\lambda_C}{\eta}\right), s_M r\rho\left(\frac{\lambda_C}{\eta}\right)^2\right\}.$$

Proof Setting the right hand side of the tumor cell equation (19) equal to zero and evaluating at the tumorous equilibrium implies that

$$T^* = \frac{\lambda_C}{\eta}. \tag{20}$$

For the MDSC equation (1c), we find that

$$M^* = \frac{1}{d_M}\left(s_M C^* + \alpha\frac{C^*}{q + C^*}\right), \tag{21}$$

which is positive depending on whether C^* is positive.

The T cell equation (1b) yields

$$\frac{a_T + s_T T^* C^*}{1 + \rho T^*(T^* + \epsilon_C C^*)} - rT^* M^* - d_T T^* = 0, \tag{22}$$

which, when we substitute (20) and (21) and rearrange, becomes a degree-3 polynomial in C^*,

$$a_3 C^{*3} + a_2 C^{*2} + a_1 C^* + a_0 = 0, \tag{23}$$

where

$$a_3 = -\frac{\rho\epsilon_C s_M r}{d_M}\left(\frac{\lambda_C}{\eta}\right)^2, \tag{24a}$$

$$a_2 = -\left(\frac{\lambda_C}{\eta}\right)\left[\left(\frac{s_M r}{d_M}\right)\left(\rho\left(\frac{\lambda_C}{\eta}\right)^2 + \rho\epsilon_C q\left(\frac{\lambda_C}{\eta}\right) + 1\right) + \rho\epsilon_C\left(\frac{\lambda_C}{\eta}\right)\left(d_T + \frac{\alpha r}{d_M}\right) - s_T\right], \tag{24b}$$

$$a_1 = -\left(\frac{\lambda_C}{\eta}\right)\left[\frac{r}{d_M}(\alpha + s_M q) + d_T\right]\left[1 + \rho\left(\frac{\lambda_C}{\eta}\right)^2\right]$$

$$- \rho\epsilon_C d_T q \left(\frac{\lambda_C}{\eta}\right)^2 + q s_T \left(\frac{\lambda_C}{\eta}\right) + a_T, \tag{24c}$$

$$a_0 = q\left[a_T - d_T\left(\frac{\lambda_C}{\eta}\right)\left(1 + \rho\left(\frac{\lambda_C}{\eta}\right)^2\right)\right]. \tag{24d}$$

We observe that a_3 is always negative since all the parameters are positive. Since a_3 is negative, when we require a_0 to be positive, the number of sign changes is odd regardless of the signs of the coefficients a_1 and a_2. Therefore, by Descartes' rule of signs, there is at least one positive zero for (23). Thus, a tumorous equilibrium is guaranteed to exist under the condition that

$$a_T > d_T\left(\frac{\lambda_C}{\eta}\right)\left(1 + \rho\left(\frac{\lambda_C}{\eta}\right)^2\right). \tag{25}$$

Now, assuming a_0 is positive and a_3 is negative, (23) has exactly one positive root, except when a_2 is positive and a_3 is negative, in which (23) has at most three positive roots. Therefore, if we desire uniqueness, it is sufficient to find conditions to require $a_2 < 0$. Since $(s_T\lambda_C/\eta)$ is the only positive term in a_2, it will be negative as long as any of the negative terms have larger magnitude than $(s_T\lambda_C/\eta)$. Therefore, $a_2 < 0$ is satisfied if

$$s_T d_M < \max\left\{s_M r,\ \rho\epsilon_C\alpha r\left(\frac{\lambda_C}{\eta}\right),\ \rho\epsilon_C d_T d_M\left(\frac{\lambda_C}{\eta}\right),\right.$$
$$\left. s_M r\rho\epsilon_C q\left(\frac{\lambda_C}{\eta}\right),\ s_M r\rho\left(\frac{\lambda_C}{\eta}\right)^2\right\}. \tag{26}$$

Since $a_2, a_3 < 0$ and $a_0 > 0$, there is only one sign change, so according to Descartes rule of signs, C^* is unique. Thus, M^* is unique. Therefore, there exists a unique tumorous equilibrium $(C^*, \lambda_C/\eta, M^*)$. □

While only one of the conditions listed in (26) is necessary to obtain uniqueness of the tumorous equilibrium, notice that each of these conditions require that tumor growth and/or immune suppression to be larger than the immune response. Thus, we can obtain uniqueness as long as any of the following are adequately larger than T cell stimulation: immunosuppression by MDSCs, inhibition by the PD-L1-PD-1 complex, heightened tumor growth, increased T cell death rate, and/or decreased T cell kill rate. This is balanced with the previous condition (25) which states that T cell activation has to be larger than immune suppression. Thus, by having a sufficient balance between the immune activation/stimulation and immune suppression, we can obtain a unique tumorous equilibrium.

Next, we determine conditions for the stability of the tumorous equilibrium when tumor growth is represented exponentially.

Theorem 6 (Stability of tumorous equilibrium) *The tumorous equilibrium, $(C^*, \lambda_C/\eta, M^*)$, for the system (1b)–(1c), (19) is locally asymptotically stable when $\rho\left(\frac{\lambda_C}{\eta}\right)^2 \geq 1$, $q > 1$, and $g > \frac{r}{d_M}\left(\frac{\lambda_C}{\eta}\right)(s_M + \alpha)$.*

Proof The Jacobian evaluated at the tumorous equilibrium is

$$J\left(C^*, T^*, M^*\right) = \begin{pmatrix} 0 & -\eta C^* & 0 \\ g & k & -r\frac{\lambda_C}{\eta} \\ s_M + \alpha\frac{q}{(q+C^*)^2} & 0 & -d_M \end{pmatrix}, \tag{27}$$

where

$$g = \frac{T^*(s_T(1+\rho {T^*}^2) - a_T\rho\epsilon_C)}{(1+\rho T^*(T^*+\epsilon_C C^*))^2}, \tag{28a}$$

$$k = \frac{(s_T(1-\rho {T^*}^2) - a_T\rho\epsilon_C)C^* - 2a_T\rho T^*}{(1+\rho T^*(T^*+\epsilon_C C^*))^2} - rM^* - d_T, \tag{28b}$$

and we have substituted (20) into the $(1,1)$- and $(2,3)$-entries to simplify the expression.

When we require

$$\rho {T^*}^2 = \rho\left(\frac{\lambda_C}{\eta}\right)^2 \geq 1, \tag{29}$$

k is guaranteed to be negative.

The characteristic polynomial of $J(C^*, T^*, M^*)$ is

$$x^3 + (d_M - k)x^2 + \Big(g\eta C^* - kd_M\Big)x + \left[d_M g\eta - r\lambda_C\left(s_M + \alpha\frac{q}{(q+C^*)^2}\right)\right]C^*. \tag{30}$$

A monic polynomial is defined to be Hurvitz if $\mathrm{Re}(x_i) < 0$ for all roots $x_i \in \mathbb{C}$. By the Routh–Hurvitz Criterion, a polynomial $p(x) = x^3 + b_1x^2 + b_2x + b_3$ is Hurvitz if and only if $b_i > 0$ for $i = 1, 2, 3$, and $(b_1b_2 - b_3) > 0$.

Under the condition (29), it follows that

$$b_1 = d_M - k > 0. \tag{31}$$

Assuming $q > 1$, we have that $q < (q+C^*)^2$, and hence $\frac{-1}{(q+C^*)^2} > -1$. Dividing b_3 by η we have

$$\begin{aligned} \frac{b_3}{\eta} &= \left[d_M g - r\left(\frac{\lambda_C}{\eta}\right)\left(s_M + \alpha\frac{q}{(q+C^*)^2}\right)\right]C^* \\ &> \left[d_M g - r\left(\frac{\lambda_C}{\eta}\right)(s_M + \alpha)\right]C^*. \end{aligned} \tag{32}$$

So, under the condition that

$$g > \frac{r}{d_M}\left(\frac{\lambda_C}{\eta}\right)(s_M + \alpha) > 0, \tag{33}$$

we have that $b_3/\eta > 0$, and hence $b_3 > 0$.

Since $g > 0$ by condition (33), then we obtain

$$b_2 = g\eta C^* - kd_M > 0. \tag{34}$$

Finally, we shall address the positivity of $(b_1b_2 - b_3)$,

$$\begin{aligned} b_1b_2 - b_3 &= (d_M - k)(g\eta C^* - kd_M) - \left[d_M g\eta - r\lambda_C\left(s_M + \alpha\frac{q}{(q+C^*)^2}\right)\right]C^* \\ &= -kd_M^2 + k^2 d_M - kg\eta C^* + r\lambda_C C^*\left(s_M + \alpha\frac{q}{(q+C^*)^2}\right) > 0, \end{aligned} \tag{35}$$

since $k < 0$ by condition (29) and $g > 0$ by condition (33).

Since $b_i > 0$ for $i = 1, 2, 3$ and $(b_1b_2 - b_3) > 0$, the characteristic polynomial (30) is Hurvitz. Therefore, the tumorous equilibrium is locally asymptotically stable under the conditions (29), (33), and $q > 1$. □

Condition (29) implies that, to obtain local stability of the tumorous equilibrium, the tumor growth rate and the inhibition by PD-L1-PD-1 need to be adequately larger than the T cell kill rate. For the condition $q > 1$, since q is the number of tumor cells at which the MDSC production occurs at half maximal rate, this is likely to occur when there is more one tumor cell, so requiring $q > 1$ is trivial.

We conclude our discussion by considering conditions for the global stability of the tumor-free equilibrium $(0, T_0^*, 0)$ for the full model (1) with logistic growth.

Theorem 7 (Global stability of tumor-free equilibrium) *The system* (1) *has a globally stable tumor-free equilibrium when* $\lambda_C < \eta\beta$, *where* $\beta := a_T/(1 + \rho\widehat{T}(\widehat{T} + \epsilon_C\widehat{C}))(r\widehat{M} + d_T)$ *and* $\widehat{C}$, $\widehat{T}$, *and* $\widehat{M}$ *are the upper bounds for glioma cells* (5), *T cells* (11), *and MDSCs* (14), *respectively, as determined in Theorem 2.*

Proof From Theorems 1–2, we have that $C(t)$, $T(t)$, and $M(t)$ are bounded above with upper bounds denoted by $\widehat{C}$, $\widehat{T}$, and $\widehat{M} > 0$, respectively, and below by 0. By these bounds,

$$\frac{dT}{dt} \geq \gamma - (r\widehat{M} + d_T)T, \tag{36}$$

where we define

$$\gamma := \frac{a_T}{1 + \rho\widehat{T}(\widehat{T} + \epsilon_C\widehat{C})}. \tag{37}$$

Thus, using a standard comparison argument,

$$\liminf_{t\to\infty} T(t) \geq \beta > 0. \tag{38}$$

where we define

$$\beta := \frac{\gamma}{r\widehat{M} + d_T}. \tag{39}$$

If $\lambda_C < \eta\beta$, then for all $s > 0$ sufficiently large,

$$\lambda_C - \eta T(s) < 0, \tag{40}$$

which, taking the limit of (2), implies that

$$\lim_{t\to\infty} C(t) = C(0) \lim_{t\to\infty} \exp\left(\int_0^t (\lambda_C - \eta T(s)) - \lambda_C \frac{C(s)}{C_{\max}} ds\right) = 0. \tag{41}$$

Bounding $T(t)$ in the tumor cell equation (1a), we have

$$\lambda_C C\left(1 - \frac{C}{C_{\max}}\right) - \eta\widehat{T}C \leq \frac{dC}{dt} \leq \lambda_C C\left(1 - \frac{C}{C_{\max}}\right), \tag{42}$$

which, taking the limit as $t \to \infty$, implies that $dC/dt \to 0$. Now, using (41),

$$\frac{dM}{dt} \leq \epsilon - d_M M(t), \tag{43}$$

where $\epsilon \to 0$ as $t \to \infty$. A standard comparison argument reveals that

$$\limsup_{t\to\infty} M(t) \leq \frac{\epsilon}{d_M}, \tag{44}$$

for any $\epsilon > 0$. Thus, since $M(t)$ is non-negative for all $t \geq 0$, $M(t) \to 0$ as $t \to \infty$, and hence, $dM/dt \to 0$ as $t \to \infty$.

Since T is bounded above and below and since $C(t) \to 0$ and $M(t) \to 0$ as $t \to \infty$, the limiting equation of (1b) is $dT/dt = G(T)$, where

$$G(T) := \frac{a_T}{1 + \rho T^2} - d_T T, \tag{45}$$

and we note that $G(T_0^*) = 0$. Since

$$G(T) - \epsilon_t \leq \frac{dT}{dt} \leq G(T) + \epsilon_t, \tag{46}$$

where $\epsilon_t \to 0$ as $t \to \infty$, using a comparison argument,

$$T_0^* - \epsilon_t \leq T(t) \leq T_0^* + \epsilon_t. \tag{47}$$

Thus, $T(t) \to T_0^*$ as $t \to \infty$, and $dT/dt \to G(T_0^*) = 0$ as $t \to \infty$.

This allows us to conclude that the tumor-free equilibrium point, $(0, T_0^*, 0)$, is globally stable in $\mathbb{R}_0^+ \times \mathbb{R}_0^+$ under the condition that $\lambda_C < \eta\beta$, where $\beta := \gamma/(r\widehat{M} + d_T)$.

□

4 Parameter Analysis

In this section, we analyze the parameter space and its effect on system (1) by implementing the Approximate Bayesian Computation (ABC) rejection method, plotting numerical simulations, and performing global sensitivity analysis using the extend Fourier Analysis Sensitivity Test (eFAST). Procedures for the ABC method, numerical simulations, and eFAST are described in Subsections 4.1, 4.2, and 4.3, respectively, and Subsection 4.4 contains an examination of the results.

We focus on finding parameter values that are specific to GBM and the experimental data in Section 2.1. Certain parameter values, such as for r, s_T, and s_M, were absent from the literature, while other values reported in Table 1 were not specific to GBM. For example, the MDSC expansion coefficient (α) represented MDSC expansion within the spleen instead of the tumor in Shariatpanahi et al (2018), and the value of the kill rate of T cells (η) was initially estimated in a model for leukemia (Kuznetsov et al (1994)). Although the experimental data was noisy and sparse, the ABC rejection method in combination with eFAST provides probability distributions of parameter estimates with a quantification of uncertainty and preliminarily identifies interactions between parameters, which subsequently can be made more precise with additional data.

4.1 Approximate Bayesian Computation

Commonly, deterministic approaches, like the gradient descent method, are used to estimate a single set of parameter values which optimally represent the given data (Allmaras et al (2013)). This optimization is computed by minimizing error between the numerical simulation and data points. However,

depending on the initial guesses of these parameters, this method can converge to different local error minima, making it difficult to uncover a set of parameter estimates which is globally optimal. To remedy this error minima ambiguity, we utilize the Approximate Bayesian Computation (ABC) rejection method (Sunnåker et al (2013), Liepe et al (2014)). This algorithm produces probability distributions of the parameter values which can indicate a range of near-optimal values for each parameter. Its use in studying complex biological systems has been increasing in recent years (Browning et al (2017), Stepien et al (2019), Xiao et al (2021), da Costa et al (2018)).

The first step of the ABC rejection method is to specify a prior distribution for each of the parameters. Consequently, we generate 1 million parameter sets, i.e., 1 million 13-dimensional vectors, where each vector forms a parameter set

$$\{\lambda_C,\ C_{\max},\ \eta,\ a_T,\ s_T,\ \rho,\ \epsilon_C,\ r,\ d_T,\ s_M,\ \alpha,\ q,\ d_M\}.$$

The values for each parameter were chosen uniformly from the ranges shown as the bounds of the horizontal axes in Fig. 3.

The second step of the ABC rejection method is to calculate the difference between the numerical simulation of the system (1) using a single parameter set and the experimental data. Quantification of the difference is determined by calculating the relative error

$$E = \frac{1}{n}\sum_{i=1}^{n}\frac{|d_i - x_i|}{d_i}, \tag{48}$$

where d_i is the experimental data point and x_i is the simulated value at the ith time point. We set d_i to be the average cell count for the ith time point, where the time points were days 7, 13, 20, 24, 27, and 34. The relative error for tumor cells (E_C), T cells (E_T), and MDSCs (E_M), is calculated individually and the total error is $E_{\text{total}} = E_C + E_T + E_M$.

The third step of the ABC rejection method is to specify an error threshold, R: if the error calculated from a simulation with a parameter set is less than the threshold, the parameter set is accepted (i.e., the simulation is sufficiently close to the experimental data), but if it is greater than the threshold, the parameter set is rejected. Since we observed visually that parameter sets that matched the tumor cell and MDSC data well often did not match the T cell data very well, we set error thresholds separately for each cell type. In particular, we set $R_C = 0.75$ for the tumor cell error threshold, $R_T = 0.72$ for the T cells, and $R_M = 0.78$ for the MDSCs. For a parameter set to be accepted, we required $E_C \leq R_C$, $E_T \leq R_T$, and $E_M \leq R_M$. Of the 1 million parameter sets sampled, we accepted about 44,000 sets, giving posterior distributions that represent the distributions of optimal parameter values for the experimental data set.

To determine whether our results were robust, we extracted different percentages of the accepted parameters and compared parameter distributions.

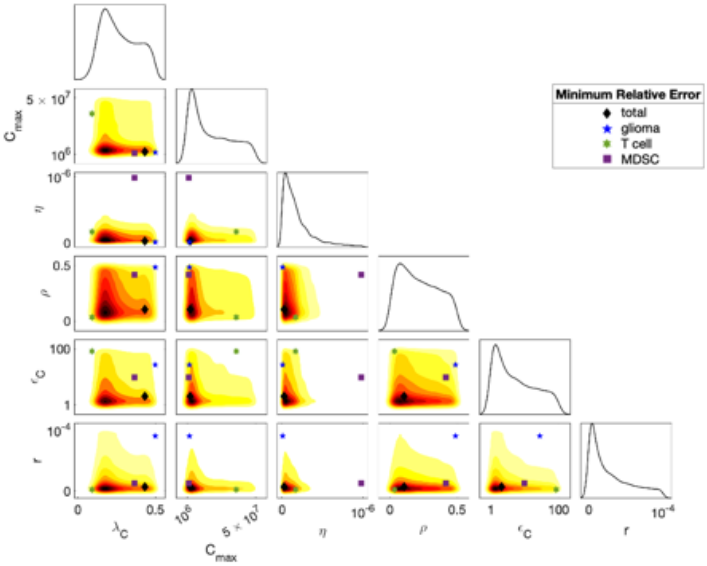

(a)

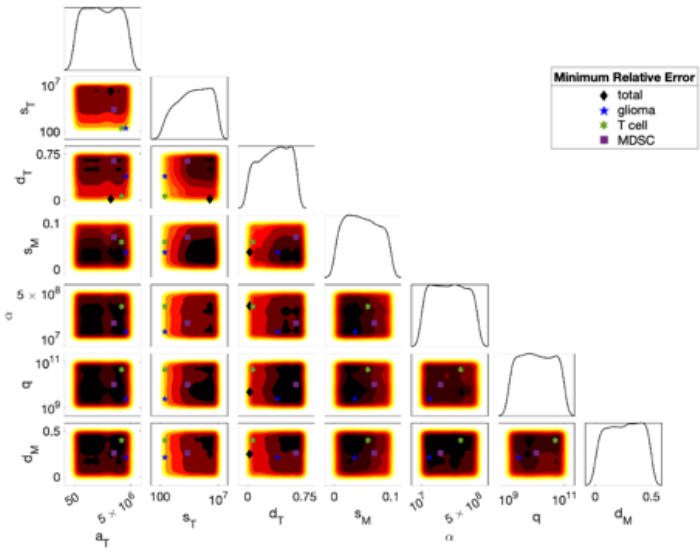

(b)

Fig. 3: ABC rejection method: The smoothed histograms for the 1D projections of the posterior distributions of each parameter along the diagonal and the 2D contour plot projections for pairs of parameters below the diagonal were produced using the smallest 25% (in terms of the total relative error E_{total} (48)) of the accepted parameter values. Darker red indicates a higher frequency of parameter values within that area. The markers indicate the parameter sets with the smallest total relative error (E_{total}), tumor cell relative error (E_C), T cell relative error (E_T), and MDSC relative error (E_M).

Table 2: Parameter summary statistics obtained from the ABC rejection method using the smallest 25% (in terms of the total relative error E_{total} (48)) of the accepted parameters.

Parameter	Mean	Median	Mode	Standard Deviation
Glioma Cells				
λ_C	0.272	0.250	0.174	0.114
$C_{\max}$	1.87×10^7	1.45×10^7	4.19×10^6	1.48×10^7
η	1.84×10^{-7}	1.27×10^{-7}	4.03×10^{-8}	1.86×10^{-7}
T Cells				
a_T	2.48×10^6	2.45×10^6	1.98×10^6	1.45×10^6
s_T	5.73×10^6	5.91×10^6	8.79×10^6	2.63×10^6
ρ	0.223	0.207	0.0768	0.142
ϵ_C	37.5	31.1	7.00	29.3
r	2.85×10^{-5}	1.83×10^{-5}	3.60×10^{-6}	2.76×10^{-5}
d_T	0.402	0.415	0.656	0.213
Myeloid-Derived Suppressor Cells				
s_M	0.0492	0.0480	0.0249	0.0278
α	2.52×10^8	2.53×10^8	8.27×10^7	1.42×10^8
q	5.09×10^{10}	5.03×10^{10}	3.89×10^{10}	2.83×10^{10}
d_M	0.258	0.263	0.419	0.143

Distributions remained largely unchanged when we analyze any percentage of our accepted parameters.

To visualize the posterior distributions, we projected the distributions down to one and two dimensions. Along the diagonal of Fig. 3a are smoothed histograms for parameters exhibiting a right-skewed distribution, while Fig. 3b shows the remaining parameters. Below the diagonal of both of these figures are the two-dimensional projections of pairs of parameters. Red shaded areas correspond with higher frequency, where higher frequency corresponds with the parameter value being sampled in the posterior distribution more often.

Parameters which exhibit a uniform posterior distribution based on the Kolmogorov-Smirnov test include the activation rate of T cells (a_T), the MDSC expansion coefficient (α), and the steepness coefficient of the MDSCs production curve (q). Posterior distributions that are right skewed include the tumor growth rate (λ_C), the tumor carrying capacity ($C_{\max}$), the tumor kill rate by T cells (η), T cell inhibition by PD-L1-PD-1 (ρ), tumor upregulation of PD-L1 (ϵ_C), and the suppression by (r). The remaining posterior distributions are negligibly skewed. Table 2 lists the mean, median, mode, and standard deviation of each distribution produced by the ABC method.

4.2 Numerical Simulations

Since mice were orthotopically implanted with 35,000 KR158 glioma cells in the experiments (Section 2.1), myeloid-derived suppressor cells (MDSCs) are

Table 3: Parameter set with the smallest error (in terms of the total relative error E_{total}) from the ABC rejection method used to fit to the minimum, average, and maximum data points.

Parameter	Minimum	Average	Maximum
Glioma Cells			
λ_C	0.0437	0.431	0.274
$C_{\max}$	4.18×10^{7}	3.04×10^{6}	4.20×10^{6}
η	9.67×10^{-7}	2.57×10^{-8}	4.63×10^{-10}
T Cells			
a_T	1.73×10^{6}	3.26×10^{6}	1.45×10^{6}
s_T	1.16×10^{6}	8.56×10^{6}	1.91×10^{6}
ρ	0.492	0.107	7.36×10^{-3}
ϵ_C	88.4	16.2	21.1
r	4.28×10^{-5}	6.92×10^{-6}	9.76×10^{-6}
d_T	0.225	0.0221	0.149
Myeloid-Derived Suppressor Cells			
s_M	2.47×10^{-3}	0.0372	0.0619
α	3.59×10^{8}	3.60×10^{8}	4.22×10^{8}
q	6.89×10^{10}	3.51×10^{10}	9.43×10^{10}
d_M	0.210	0.251	0.360
Error (E_{total})	1.78	0.785	0.937

absent from the brain before the introduction of a tumor, and the number of activated T cells are initially negligible, the initial conditions for the simulations were set to be $C(0) = 35,000$, $T(0) = 0$, and $M(0) = 0$ cells. We assume that any loss of glioma cells due to implantation is negligible. Numerical simulations were run using the parameter values listed in Tables 2–3. Data points for glioma cells, T cells, and MDSCs are plotted alongside the numerical simulations in Fig. 4.

In Fig. 4a, we plotted a numerical simulation using the mean parameter values listed in Table 2, and then in the other simulations, shifted each parameter individually up and down by its standard deviation. Fig. 4a illustrates that our model was able to capture most data points within one standard deviation from the mean.

The ABC rejection method results shown in Fig. 3 were produced by using the average data point at each time step when calculating the relative error (48), but we also used the minimum data point at each time step and the maximum data point to run the ABC rejection method in two separate instances. The parameter sets with minimal error are listed in Table 3 along with their total error values, and numerical simulations are shown in Fig. 4b. A comparison of their total error values could suggest that our parameter ranges are better suited for larger gliomas (error: 0.937) rather than smaller gliomas (error: 1.78), while they are best suited for the average glioma size (error:

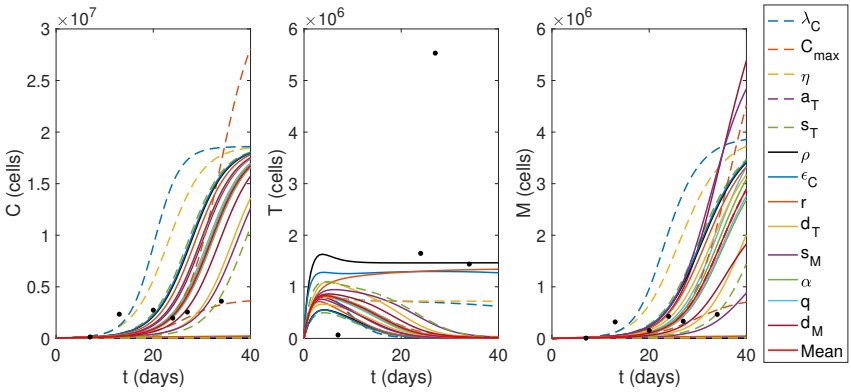

(a)

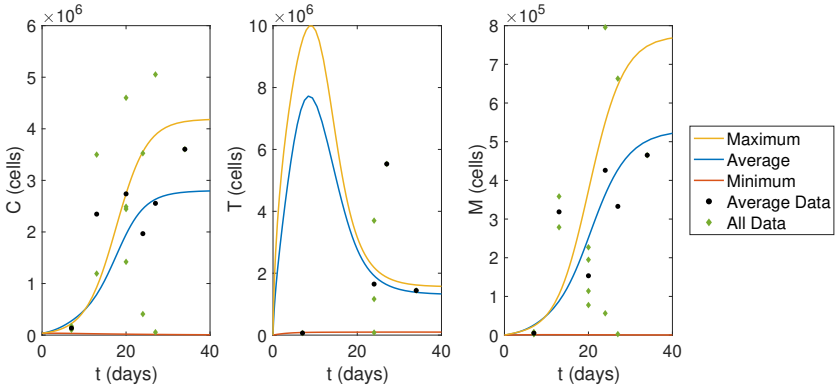

(b)

Fig. 4: Numerical simulations after implanting 35,000 glioma cells. (a) The "Mean" simulation used the "Mean" parameter value found using the ABC rejection method as listed in Table 2. In the remaining simulations, we shifted a single parameter value up and down by its standard deviation listed in Table 2. While shifting most parameters resulted in the ultimate decay of T cells, and thus a suppressed immune response, decreasing the immunosuppression via MDSCs (r) and the PD-L1-PD-1 complex (ρ and ϵ_C) seemed to stabilize the number of T cells. Increasing the stimulation of T cells (s_T) and the T cell kill rate of tumor cells (η) also had this effect but to a lesser extent. (b) The maximum, average, and minimum curves represent the simulations using the parameter sets of minimal error found using the ABC rejection method with respect to the maximum, average, and minimum data point at time step as listed in Table 3.

0.785). However, these differences in error could also be explained by the variability in the data.

4.3 Sensitivity Analysis

To determine the influence of parameters on tumor progression, we conducted a sensitivity analysis using the extended Fourier Analysis Sensitivity Test (eFAST) method outlined in Saltelli et al (1999) by utilizing the MATLAB code developed by the Kirshner Lab at the University of Michigan (Kirschner and Panetta (1998); Kirschner (2008)). eFAST is a global sensitivity analysis method which neither requires model linearity nor a monotonic relationship between the output and the parameters (Saltelli et al (2008)). Similar to the Sobol' method, it is a variance-based method, but it uses a monodimensional Fourier expansion of the model to evaluate variance. Because of this monodimensional transformation, each parameter i can be sampled within the unit hypercube by varying $s \in (-\pi, \pi)$ along the space-filling search curve, x_i, defined by

$$x_i(s) = G_i(\sin(\omega_i s + \varphi_i)), \tag{49}$$

where ω_i is the angular frequency assigned to parameter i, φ_i is a random phase-shift, and G_i is a transformation function determined by parameter i's probability distribution. By having multiple resamplings of this search curve, φ_i increases the randomness of the samples. The assigned angular frequency, ω_i, can later be used to extract the variance that parameter i contributes to the system.

The probability distribution of parameter i is used to determine the transformation function, G_i, hence the search curve, x_i. For parameters with right-skewed posterior distributions from the ABC method (λ_C, $C_{\max}$, η, ρ, ϵ_C, and r), we used the following search curve proposed by Cukier et al (1973),

$$x_i = n_i \exp(v_i \sin(\omega_i s + \varphi_i)), \tag{50}$$

where n_i is the nominal value of the ith parameter and v_i accounts for uncertainty by altering the width of the parameter range. The nominal value, n_i, was chosen to be parameter i's most frequently accepted value by the ABC method, i.e. the mode of the posterior distribution. We specify v_i to be such that parameters are sampled within the interval $[0, 1]$ (and later translate them to the intervals shown as the bounds of the horizontal axes in Fig. 3), which can be done by choosing $v_i = \ln(1/n_i)$.

For the remaining parameters (a_T, s_T, d_T, s_M, α, q, d_M), we used the search curve for a uniform distribution that was determined by Saltelli et al (1999),

$$x_i = \frac{1}{2} + \frac{1}{\pi}\arcsin(\sin(\omega_i s + \varphi_i)). \tag{51}$$

Using these search curves, we chose to generate 2,049 parameter sets for each 5 resamplings, which resulted in a total sample size of 10,245 parameter sets. For information on how we chose the sample size and number of resamplings, see Appendix C. After parameters were sampled from the unit hypercube, the samples for each parameter were translated to the ranges shown as the bounds of the horizontal axes in Fig. 3.

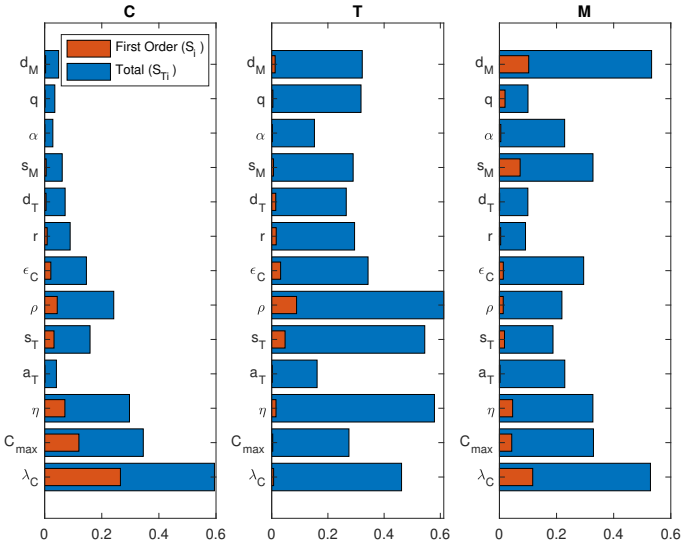

(a) Each parameter was sampled uniformly using (51).

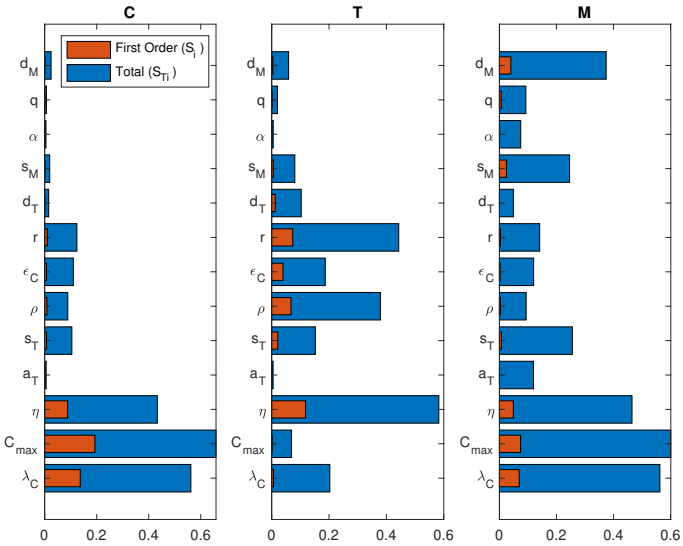

(b) Parameters λ_C, $C_{\max}$, η, ρ, ϵ_C, and r were sampled using (50), while the remaining were sampled uniformly using (51).

Fig. 5: Global sensitivity analysis: The eFAST method was used to calculate the main effect S_i and total effect S_{Ti} of each parameter on tumor cells (C), T cells (T), and MDSCs (M) at $t = 40$ days. Given the posterior distributions in Fig. 3, the true sensitivity indices are expected to lie between the results in (a) and (b).

The main effect, S_i, otherwise known as the first-order index, describes the effect that a single parameter x_i has on the variance of the system independently of other parameters. In contrast, the total effect index, S_{Ti}, is a sum of the parameter's first-order index S_i as well as higher-order interactions of x_i with other parameters. Thus, for every parameter x_i, $S_{Ti} \geq S_i$. In Fig. 5, we illustrate the main effect S_i and the total effect index S_{Ti} for each parameter calculated after a simulation time of 40 days. The larger the difference between S_{Ti} and S_i, the more interaction there is between x_i and other parameters in influencing the variance of the output.

In Fig. 5b, we sampled the previously specified parameters (λ_C, $C_{\max}$, η, ρ, ϵ_C, and r) using the right-skewed sampling technique with the search curve (50) of Cukier et al (1973) to compare to the standard uniform sampling technique with the search curve (51) shown in Fig. 5a. Since the search curve of Cukier et al (1973) produces a more significant right-skew than our ABC distributions suggest (Fig. 3), we assume that the actual sensitivity indices are within the range produced by the results shown in Fig. 5a and 5b.

We show the sensitivity results in Fig. 5 at $t = 40$ days, the approximate time at which an untreated mouse requires euthanasia, but note that the sensitivity results on days 60, 80, and 100 were qualitatively similar. When we compared the results in Fig. 5 to sensitivity results on days 5, 10, and 20, results were generally similar but had a few differences. For example, each cell population becomes increasingly sensitive to the tumor carrying capacity ($C_{\max}$) as time progresses. This result is to be expected since limited space and nutrients will become more significant for larger tumors. MDSCs are initially very sensitive to the MDSC recruitment rate (s_M), but this decreased with time and, by day 40, its influence is surpassed by the MDSC death rate (d_M). This result suggests that a CCR2 antagonist should be used as soon as possible, and if the tumor is in its later stages, therapeutics that kill MDSCs at the tumor site should be considered instead. T cells began as most sensitive to the inhibition rate by PD-L1-PD-1 (ρ) for both sampling methods, but for the right-skewed sampling method, this switched to T cells being the most sensitive to the tumor kill rate by T cells (η) by day 10. Further, for this sampling method, T cells sensitivity to the inhibition rate by MDSCs (r) continues to increase until it surpasses ρ by day 20, where it remains the second most influential parameter. By comparison, when using the uniform search curve, the T cells start as noticeably more sensitive to the inhibition by PD-L1-PD-1 (ρ) than all other parameters, and while the variance due to the other parameters increases over time, ρ remains the most sensitive parameter. This proposes that treatment with an immune checkpoint inhibitor, such as anti-PD-1 or anti-PD-L1, should be beneficial at any time, but it is best to treat sooner if possible.

When we compare Fig. 5a and 5b, the uniform sampling method in Fig. 5a shows more interaction between parameters for all three cell populations but especially for T cells. This would suggest that many parameters need to be targeted therapeutically to control the populations. Fig. 5b thus helps us to

narrow our potential targets by showcasing less interactions between parameters and highlighting only the essential ones. For the cancer population, the uniform sampling method suggests that the most important targets are, in order of importance, the tumor growth rate (λ_C), the tumor carrying capacity ($C_{\max}$), and the tumor kill rate by T cells (η). The right-skewed sampling method also highlights these three, but suggests that the cancer population is more sensitive to the tumor carrying capacity ($C_{\max}$) than the tumor growth rate (λ_C). This sampling method additionally suggests that T cells are most sensitive to the tumor kill rate by T cells (η) as well as inhibition by MDSCs (r) and the PD-L1-PD-1 complex (ρ). In contrast, the uniform sampling method marks inhibition by PD-L1-PD-1 (ρ) to be the most important parameter followed by the tumor kill rate by T cells (η) and the stimulation of T cells (s_T). For MDSCs, the uniform sampling method shows model sensitivity to the MDSC death rate (d_M) and the tumor growth rate (λ_C), although there is also a comparably large first order index (S_i) for the MDSC recruitment rate (s_M). This is similar to the right-skewed sampling results, although Fig. 5b also includes the tumor kill rate by T cells (η) and the tumor carrying capacity ($C_{\max}$) with the latter being the most influential on MDSC variance. Lastly, notice in Fig. 5b, all cell populations are insensitive to the steepness coefficient of the MDSC production curve (q), the MDSC expansion coefficient (α), and the activation rate of T cells (a_T), while the uniform sampling method shows some sensitivity, albeit slight, towards these parameters for the T cell and MDSC populations.

While these differences show the importance of considering probability distributions when determining a sampling curve, the distributions for λ_C, $C_{\max}$, η, ρ, ϵ_C, and r were not as right-skewed as the sampling curve (50). So, in our case, we should consider the combined results of Fig. 5a and 5b. Collective results show that T cells are sensitive to perturbations in several parameters, including the kill rate of tumor cells by T cells (η) as well as the inhibition of T cells by PD-L1-PD-1 (ρ) and MDSCs (r). Tumor cells express sensitivity to the tumor growth rate (λ_C), tumor carrying capacity ($C_{\max}$), and the kill rate by T cells (η). These results are similar for the MDSC population, however, the death rate (d_M) and recruitment rate of MDSCs (s_M) hold a significantly larger influence on variations. Also, while MDSCs and tumor cells display similar total order indices (S_{Ti}) for the tumor kill rate by T cells (η) and the tumor growth rate (λ_C), the first order indices (S_i) of these parameters are larger for tumor cells than MDSCs. This is most likely since these parameters directly influence the tumor cell population but indirectly affect the MDSC population.

4.4 Results

One of the parameters for which we could find no estimates for its value in existing literature was the recruitment rate of MDSCs due to the chemokines CCL2 and CCL7, s_M. From the posterior distribution found using the ABC

method, we expect that the value of s_M will fall within the range of 0.0214–0.0770 day^{-1} (Table 2). Separately, we calculated an approximation of s_M using data on the expression levels of CCL2 in KR158 glioma cells as well as the effect of CCL2 on MDSC migration in vitro (see Supplementary Information). From the data, we calculated that the recruitment rate of MDSCs due to CCL2 expression on KR158 glioma cells is between 0.0123–0.0144 MDSCs per day per tumor cell. Since this data only included the effect of CCL2 and not CCL7 on MDSC migration, we expect this range to be an underestimate for s_M. However, as the mode of the s_M distribution, 0.0249, found using the ABC method (Table 2) is close to double the experimentally calculated value, we expect that CCL7 will have a similar effect on MDSC migration as CCL2, assuming that the interaction between CCL2 and CCL7 causes an additive effect in recruitment.

The range for the MDSC expansion coefficient (α) stated in Table 1 was obtained from studies considering MDSC overproduction in the spleen due to the presence of a tumor (Cao et al (2016); Srivastava et al (2012)). We used the values for α associated with breast and lung cancer, since these are solid tumors like glioblastoma. We anticipated the distribution for α using the ABC method to be right-skewed since that would suggest that the glioma only recruits a smaller portion of the MDSCs produced in the spleen. However, the posterior distribution for α in Fig. 3b was uniform instead of right-skewed, potentially suggesting that gliomas are able to recruit most of the MDSCs produced in the spleen. It could also mean that the presence of a glioma causes more MDSC overproduction in the spleen than a breast or lung tumor. More detailed data would need to be collected to corroborate these possibilities.

When we consider the eFAST results, large differences between the total effect indices (S_{Ti}) and the first-order indices (S_i) show that significant interaction is occurring between parameters resulting in a synergistic effect on the variance of the tumor-immune system. In all three populations, the tumor growth rate (λ_C), tumor carrying capacity ($C_{\max}$), and the tumor kill rate by T cells (η) are fairly sensitive parameters which exhibit interactions with other parameters. Although eFAST displays this, it does not identify which parameters are interacting with each other. By combining eFAST with the contour plots from the ABC rejection method in Fig. 3a, we can make inferences about potential relationships. Notice that there is a considerable inverse relationship between λ_C with the inhibition rate by PD-L1-PD-1 (ρ) and the tumor upregulation of PD-L1 (ϵ_C), $C_{\max}$ with ρ, ϵ_C, and the inhibition by MDSCs (r), as well as η with r and slightly with ϵ_C. Although it would be reasonable to assume that this inverse relationship is merely due to these parameters each exhibiting right-skewed distributions, observe that the inverse relationship between λ_C, $C_{\max}$, and η themselves is negligible. Therefore, we hypothesize that, although the tumor population is less sensitive to the immune suppression parameters ρ, ϵ_C, and r, targeting these could decrease the tumor's sensitivity to λ_C, $C_{\max}$,

and η. At the very least, according to the T cell sensitivity in Fig. 5b, targeting these parameters would increase the immune response, thus decreasing the tumor population.

From the ABC contour plots in Fig. 3a, there also appears to be an inverse relationship between the tumor upregulation of PD-L1 (ϵ_C) and the inhibition of T cells by the PD-L1-PD-1 complex (ρ) and by MDSCs (r). The first relationship suggests that as tumor cells express more PD-L1, the PD-L1-PD-1 complex need not be as effective at inhibition in order to produce the same outcome. The second relationship suggests that r, although it is a less sensitive parameter, helps to increase the system's sensitivity to ϵ_C. Thus, perturbations in the two forms of immunosuppression, the PD-L1-PD-1 complex and MDSCs, cause greater variance on the tumor together rather than alone.

5 Discussion and Future Directions

Current treatment paradigms for the highly aggressive primary brain tumor, glioblastoma (GBM), present limited efficacy. Many barriers, such as the highly immune suppressed tumor microenvironment, make gliomas difficult to treat. To address this barrier, we mathematically model GBM-immune dynamics by considering the role of myeloid-derived suppressor cells (MDSCs) in aiding GBM progression through T cell suppression. Gliomas recruit CCR2$^+$ MDSCs to the tumor microenvironment by expressing the chemokines CCL2 and CCL7, which are ligands of the CCR2 receptor. Once at the tumor site, MDSCs suppress T cells, which are already inhibited by the formation of the PD-L1-PD-1 complex. This complex forms due to T cell interaction with tumor cells, and it masks the tumor from identification by T cells. Incorporating these two forms of immunosuppression prepares our model for future extension to include immunotherapies and optimize treatments.

Our results reinforce pre-clinical studies by Flores-Toro et al (2020) which suggest that MDSCs and the PD-L1-PD-1 immune checkpoint should be targeted together to increase the immune response and thus decrease the tumor burden. Therefore, promising therapeutics include immune checkpoint inhibitors, such as anti-PD-1 and anti-PD-L1, and CCR2 antagonists. Time-dependent sensitivity analysis with eFAST proposes that treatment with these therapeutics should be used as soon as possible; however, an immune checkpoint inhibitor should offer some benefit at any stage. In contrast, MDSC recruitment should be blocked by a CCR2 antagonist in the early stages of a tumor, but immunotherapies which kill MDSCs at the tumor site should be considered for larger tumors.

Stability analysis of the system (1) established conditions for the existence and stability of the tumor-free and tumorous equilibria. The unique tumor-free equilibrium, $(0, T_0^*, 0)$, is corroborated by immunohistochemistry data showing the absence of MDSCs within the tumor-free mouse brain (Fig. 2). This equilibrium is locally asymptotically stable when $\lambda_C < \eta T_0^*$, i.e., the initial immune response is greater than the tumor growth rate, which is equivalent

to results in Nikolopoulou et al (2018). Further, it is globally stable when $\lambda_C(1+\rho\widehat{T}(\widehat{T}+\epsilon_C\widehat{C}))(r\widehat{M}+d_T) < \eta a_T$. This suggests that, regardless of the initial number of activated T cells, if the kill rate of tumor cells by T cells and the activation rate of T cells overcomes the tumor growth rate, immune suppression by PD-L1-PD-1 and MDSCs, and the death rate of T cells, then the system will tend to the tumor-free equilibrium. When we reduce the system to represent tumor growth exponentially, the unique tumorous equilibrium is locally asymptotically stable when the tumor growth rate and inhibition rate by PD-L1-PD-1 adequately exceed the kill rate of T cells ($\rho\lambda_C^2 \geq \eta$) and when the steepness coefficient of the MDSC production curve is sufficiently large ($q > 1$). Refer to the Supplementary Information to see conditions sufficient for the uniqueness and local stability of the tumorous equilibrium of the full model (1) with logistic growth.

We obtained estimates of the tumor volume and cell counts from murine GBM data collected from immunofluorescence imaging. T cell data was more sparse than the glioma and MDSC data, so future model predictions could be improved by incorporating more time-dependent T cell data. In general, more data would improve the predictive capabilities of the model, especially if the cell populations within a single mouse could be tracked over time.

Given the limited data set, we used the Approximate Bayesian Computation (ABC) rejection method in unison with data to obtain information on the probability distribution of realistic values within the parameter space. We identified approximate values and quantified the associated uncertainty for previously unknown parameters, such as the recruitment rate of MDSCs (s_M), and the inhibition rate of T cells by MDSCs (r). By calculating a rough estimate of s_M using chemokine expression levels on glioma cells and MDSC migration levels to certain concentrations of the chemokine CCL2 measured from the experimental data, we found that the parameter values estimated by the ABC method was of the same order as the calculation from data, thus validating our model. Further, we found that the values predicted for r were noticeably greater than the estimated tumor kill rate by T cells η (Table 2), suggesting that MDSCs suppress T cells more effectively than T cells kill tumor cells (note that this conclusion remains the case when we widen the range of η to be that of r). This would explain the difficulty T cells experience in overcoming a glioma. Further biological testing would need to occur to validate this hypothesis.

Numerical simulations in Fig. 4a were plotted using the mean and/or one standard deviation from the mean of the parameter distributions found using the ABC method. The simulations show that decreasing the upregulation of PD-L1 on tumor cells (ϵ_C) as well T cell inhibition by the PD-L1-PD-1 complex (ρ) and by MDSCs (r) caused T cells to plateau instead of descend towards 0. These findings suggest that a combination treatment which targets PD-L1, or the PD-L1-PD-1 complex in general, as well as the immunosuppressive capabilities of MDSCs would maximize the number of activated T cells at the tumor site. Decreasing the tumor growth rate (λ_C) and increasing the T

cell kill rate of tumor cells (η) also caused T cells to plateau in the tumor environment–although to a lesser extent. For MDSCs, increasing the MDSC recruitment by chemokines (s_M) and decreasing the MDSC death rate (d_M) by their standard deviations caused a noticeable increase in MDSCs by day 40. Further, both MDSCs and glioma cells exhibit a surge due to decreasing the T cell kill rate of tumor cells as well as increasing the tumor growth rate (λ_C) and carrying capacity ($C_{\max}$). Surgical resection of the tumor can decrease the tumor growth rate and carrying capacity by disrupting the influx of nutrients through damage to the vasculature. Thus, a treatment plan which includes surgery and immunotherapies that increase the function of T cells by targeting the PD-L1-PD-1 complex (potentially by targetting PD-L1) along with MDSC recruitment, inhibitory mechanisms, and/or death rate should be explored in pre-clinical models.

Parameter distributions found by using the ABC method also aided global sensitivity analysis by informing the choice of search curve by which to sample parameters with eFAST. Global sensitivity analysis in Fig. 5 indicated that there are several drivers of the system, including tumor growth rate (λ_C), the tumor carrying capacity ($C_{\max}$), and T cell kill rate (η) along with noticeable interaction occurring between parameters to affect the variance of the system. Interactions between parameters are identified by viewing differences between the total effect indices (S_{Ti}) and the first-order indices (S_i). By comparing the eFAST results with the ABC method in Fig. 3a, we hypothesize that interaction could be occurring between these three drivers and parameters representing immune suppression–namely the tumor upregulation of PD-L1 (ϵ_C) along with the inhibition by PD-L1-PD-1 (ρ) and by MDSCs (r), since there appears to be an inverse relationship between these parameters in Fig. 3a. Further, T cell sensitivity in Fig. 5 show that targeting these parameters would increase the immune response regardless of any interactions. This suggests that the PD-L1-PD-1 complex and inhibition by MDSCs should be therapeutically targeted to relieve tumor burden and increase the immune response.

Overall, there is a mutually beneficial relationship between the ABC method and eFAST. The distributions produced by ABC in accordance with data inform the choice of search curve when sampling parameters in eFAST. In return, the interaction effects displayed by eFAST direct us to look for relationships between parameters using the ABC results. Thus, the two together increase the reliability of results as well as the inferences that can be made.

Future directions include extending this model to incorporate immunotherapies targeting the PD-L1-PD-1 complex and MDSCs and then optimizing treatment regimens to minimize tumor burden. Anti-PD-1, which targets PD-1 on T cells, has not been successful as a monotherapy in part because it requires more activated T cells to be in the tumor microenvironment (Kleponis et al (2015)). Simulations in Nikolopoulou et al (2018) suggest that anti-PD-1 alone is not able to increase the number of T cells to a tumor eradication threshold. Through inhibition, MDSCs decrease the number of activated T cells. Treatment with a CCR2 antagonist decreases the recruitment of MDSCs, which

indirectly increases the number of activated T cells, thus improving the efficacy of anti-PD-1. This improved efficacy is supported by data showing increased survival rates in glioma-bearing mice treated with anti-PD-1 and the CCR2 antagonist, CCX872 (Flores-Toro et al, 2020, Fig. 4).

While anti-PD-1 prevents the formation of the PD-L1-PD-1 complex, another reasonable therapeutic target for glioblastoma is PD-L1 in addition to, or instead of, PD-1 since our results do not fully distinguish between the two. Clinically, it has been found that gliomas upregulate PD-L1 at a higher incidence compared to other tumors (Preusser et al (2015a)), further indicating the potential for targeting PD-L1. Further, anti-PD-L1 exhibits a similar toxicity profile to anti-PD-1 (Spagnuolo and Gridelli (2018)), which indicates that the treatment could be tolerated similarly. Further testing in mice would be a necessary initial step to evaluate the efficacy of anti-PD-L1 versus anti-PD-1 in combination with a CCR2 antagonist.

Statements and Declarations

Disclosure statement. The authors declare that they have no conflict of interest.

Funding. H.G.A. and G.P.T. acknowledge support from the NIH/NCATS Clinical and Translational Science Awards #UL1TR001427 and #TL1TR001428. D.C.H. acknowledges support from NIH R01GM131405-02. Y.K. acknowledges support from NSF DEB-1930728 and NIH R01GM131405-02. J.K.H. acknowledges support from the National Institute of Neurological Disorders and Stroke NS108781. T.L.S. acknowledges support from a Simons Collaboration Grant for Mathematicians (#710482) and NSF grant DMS-2151566.

Ethics approval. All procedures involving animal housing and surgical protocols were followed according to the guidelines of the University of Florida Institutional Animal Care and Use Committee.

Authors' contributions. Conceptualization and Methodology: all authors; Formal analysis, Software, Validation, and Visualization: Hannah G. Anderson; Investigation and Data Curation: Gregory P. Takacs; Resources: Jeffrey K. Harrison; Supervision: Tracy L. Stepien, Jeffrey K. Harrison, Yang Kuang; Writing - original draft preparation: Hannah G. Anderson; Writing - review and editing: all authors.

Code availability. The source code used to generate the results for this article is available through GitHub at https://github.com/stepien-lab/glioma-Tcell-MDSC [v1.0.0]. The code is platform independent and written in MATLAB.

Supplementary information. *SupplementaryMethods.pdf* contains details regarding the literature search and estimation of parameters and additional

theorems of the uniqueness and local stability of the tumorous equilibrium for system (1).

SupplementaryData.xlsx contains time-dependent data of tumor volumes and the three studied cell populations, which was collected according to the experimental methods in Appendix A.

Appendix A Experimental Setup and Image Analysis

The following appendix details the murine glioma experimental study and image analysis pipeline.

A.1 Animals

CX3CR1-deficient $CX3CR1^{GFP/GFP}$ [B6.129P-Cx3cr1tm1Litt/J]), and CCR2-deficient $CCR2^{RFP/RFP}$ [B6.129(Cg)-Ccr2tm2.1Ifc/J]) mice were obtained from The Jackson Laboratory. $CCR2^{RFP/WT}/CX3CR1^{GFP/WT}$ mice were generated via in-house breeding of homozygous $CX3CR1^{GFP/GFP}$ and homozygous $CCR2^{RFP/RFP}$ mice. All procedures involving animal housing and surgical protocols were followed according to the guidelines of the University of Florida Institutional Animal Care and Use Committee.

A.2 Cell Culture

KR158B glioma cells were cultured in Dulbecco's Modified Eagle Medium (DMEM) supplemented with 1% penicillin-streptomycin and 10% fetal bovine serum (FBS). Cells were grown in a humidified incubator at 37 °C with 5% CO2. DMEM and penicillin-streptomycin were purchased through Invitrogen. FBS was purchased through Thermo Scientific.

A.3 Orthotopic Brain Tumor Model

Animals were anesthetized using isoflurane and administered analgesia prior to cell injection. While under anesthesia, the surgical site was prepared, a 2- to 3-mm incision was made at the midline of the skull. Using a stereotaxic apparatus (Stoelting), the mice were secured, and a Hamilton syringe was positioned 2-mm lateral from the bregma. KR158B glioma cells (3.5×10^4), in a total volume of 2 μL were injected 3-mm deep into the right cerebral hemisphere using an automated microfluidic injection system (Stoelting) at a rate of 1 μL/min. Cells are suspended in a 1:1 ratio of methylcellulose to PBS. Post injection, the needle was retracted slowly, and the surgical site was closed via suture and bone wax. Animals were then placed into a warm cage for postsurgical monitoring.

A.4 Immunofluorescence

Mice were euthanized and transcardial perfusions were performed using a 10mL syringe with a 25G winged infusion set, of 20mL 4.0% paraformaldehyde (PFA) solution. Following fixative perfusion, mouse brains were removed and soaked in 4.0% PFA for 1hr. Brains were subsequently transferred to 30% sucrose solution for 24hrs and snap frozen using liquid nitrogen chilled 2-Methylbutane. Brains were embedded in optimal cutting temperature compound and mounted for cryo-sectioning (Lecia Biosystems Cryostat). 5-10μm thick sections were taken and mounted on microscope slides. Sections were dried overnight at 4C. For CD3ϵ staining, sections were brought up to room temperature and rehydrate in PBS for 5 mins. Normal goat serum (10%) blocking buffer was applied in a humidified chamber at RT for 1 hr. Rat anti-mouse CD3ϵ (Biolegend 155602) primary antibody (0.5mg/mL) was applied to each slide and stored at 4C overnight. The following day samples were washed in PBS 3 times and incubated subsequently in goat anti-rat Alexa 647(Invitrogen A21247) secondary antibody (2mg/mL). The sections were then washed 3 times with PBS, counterstained with Vectashield antifade mounting medium with 4',6- diamidino-2-phenylindole, and imaged using an inverted Nikon TiE-PFS-A1R confocal microscope. Images were post-processed using Nikon Elements software.

A.5 Cell Quantification

For each brain tumor, 3 sections were imaged using a 20x objective, quantified, and averaged prior to statistical inferences. For larger tumors, a series of 20x images were taken and stitched together using Nikon Elements software. Images were imported into Cell Profiler (Stirling et al (2021)) for quantification using an image-analysis pipeline. Briefly, the pipeline utilizes each fluorescent channel to identify and quantify DAPI-stained nuclei, $\text{CCR2}^{\text{WT/RFP}}$, $\text{CX3CR1}^{\text{WT/GFP}}$, and CD3 cells. Masks were generated for each cell identity. DAPI-stained nuclei mask was used as a prerequisite for subsequent cell identification. To identify $\text{CCR2}^{\text{WT/RFP}}/\text{CX3CR1}^{\text{WT/GFP}}$ cells "RelateObjects" command was carried out to identify co-localization of RFP and GFP positive cells. Tumor area was calculated through the cropping function with dysplastic DAPI staining denoting tumor boundary. The final output includes tumor area and numbers of each cell type.

Appendix B Data Usage

The following appendix discusses the data usage as well as statistical analyses performed.

B.1 Data Conversion

Using Cell Profiler (Stirling et al (2021)), the immunofluorescence data measured the number of MDSCs and T cells in 2D on a 0.01 mm thick slice that

was removed from the approximate center of the tumor (Appendix A.5). Since CellProfiler was not able to determine the number of tumor cells in the 2D image, we estimated this by assuming that the density of tumor cells in an epithelial tumor is approximately 10^8 cell/cm^3 (Del Monte (2009)). To convert these cell numbers in terms of a 3D tumor, we assumed that the tumor is spherical and that the average density of cells throughout the tumor is that of the slice. The tumor area on the 2D image was used to find a radius, which was then used to calculate a volume. For each of the cell types, we calculated a 2D density, and then used that along with the volume to calculate the total number of cells throughout the entire 3D tumor.

B.2 Statistical Analysis

We calculated that there were strong outliers for the number of glioma cells and MDSCs measured from two mice in the data by defining a "strong outlier" to be any value which is more than $3 \times$ IQR above/below the upper/lower quartile, respectively. Although we used these two strong outliers to create an adequate range for the carrying capacity of tumor cells, $C_{\max}$, we eliminated these two data points when running the Approximate Bayesian Computation method (Section 4.1). Since there were less T cell data points, we were unable to show the T cell data from those two mice to be outliers. This is likely why the numerical simulations in Fig. 4a are unable to capture the two largest T cell points within one standard deviation of each parameter from the mean accepted value according to the ABC method. Given more data for T cells, these data points might be considered outliers and eliminated.

Appendix C Number of samples (N_s) and resamplings (N_r)) for eFAST

Since we have 13 parameters, the minimum allowable value of $\omega_{\max}$ is 13, which results in a minimum sample size of 105. However, we can improve accuracy by choosing a larger $\omega_{\max}$ in order to increase the distance between the frequencies of the complementary set $\{\omega_{(-i)}\}$. This allows us to better obtain the spectrum of the system's Fourier series due to each frequency, i.e., we can better obtain the variance of the system due to each parameter. (Saltelli et al, 1999, Fig. 9) compared the accuracy of several samples sizes for eFAST to analytical results for total sensitivity indices (S_{Ti}) and found that a sample size of roughly 2048 (including resamplings) was more than sufficiently accurate. Therefore, we generated 2049 parameter sets for each of our resamplings. Since the sample size for each resampling is determined by

$$N_s = 2M\omega_{\max} + 1, \tag{C1}$$

where M is the interference factor (usually 4), the maximum frequency, $\omega_{\max}$, used was 256. According to the algorithm for the selection of complementary

frequencies proposed by Saltelli et al (1999), the maximum allowable frequency for the complementary set was

$$\max\{\omega_{(-i)}\} = (1/M)(\omega_{\max}/2) = 32. \tag{C2}$$

The complementary set was then chosen within the range of integers between 1 and 32 in order to maximize the step size between each frequency (in this case, the step size was 2). From experience, Saltelli et al (1999) also advised that the number of resamplings, N_r, be chosen in order to keep $\omega_{\max}/N_r$ within the range of 16 and 64. So, we chose to have 5 resamplings ($\omega_{\max}/N_r = 51.2$) where the phase shifts, φ_i, for each resampling was randomly chosen from $[0, 2\pi]$. Thus, this sampling method generated 2049 parameter sets for each of our 5 resamplings, resulting in a total sample size of 10,245 parameter sets.

References

Allahverdy A, Moghaddam AK, Rahbar S, et al (2019) An agent-based model for investigating the effect of myeloid-derived suppressor cells and its depletion on tumor immune surveillance. Journal of Medical Signals and Sensors 9(1):15–23. https://doi.org/10.4103/jmss.JMSS_33_18

Allmaras M, Bangerth W, Linhart JM, et al (2013) Estimating parameters in physical models through bayesian inversion: A complete example. Society of Industrial and Applied Mathematics Review 55(1):149–167. https://doi.org/10.1137/100788604

Ansell SM, Lesokhin AM, Borrello I, et al (2015) PD-1 blockade with nivolumab in relapsed or refractory hodgkin's lymphoma. New England Journal of Medicine 372(4):311–319

Banerjee S, Khajanchi S, Chaudhuri S (2015) A mathematical model to elucidate brain tumor abrogation by immunotherapy with T11 target structure. PLoS One 10(5):e0123,611. https://doi.org/10.1371/journal.pone.0123611

Bausart M, Préat V, Malfanti A (2022) Immunotherapy for glioblastoma: the promise of combination strategies. Journal of Experimental & Clinical Cancer Research 41(1):1–22

Bitsouni V, Tsilidis V (2022) Mathematical modeling of tumor-immune system interactions: the effect of rituximab on breast cancer immune response. Journal of Theoretical Biology 539:111,001. https://doi.org/10.1016/j.jtbi.2021.111001

Brahmer J, Reckamp KL, Baas P, et al (2015) Nivolumab versus docetaxel in advanced squamous-cell non–small-cell lung cancer. New England Journal

of Medicine 373(2):123–135

Brown NF, Carter TJ, Ottaviani D, et al (2018) Harnessing the immune system in glioblastoma. British Journal of Cancer 119(10):1171–1181. https://doi.org/10.1038/s41416-018-0258-8

Browning AP, McCue SW, Simpson MJ (2017) A bayesian computational approach to explore the optimal duration of a cell proliferation assay. Bulletin of Mathematical Biology 79(8):1888–1906. https://doi.org/10.1007/s11538-017-0311-4

Bryukhovetskiy I (2022) Cell-based immunotherapy of glioblastoma multiforme. Oncology Letters 23(4):1–14

Butner JD, Wang Z, Elganainy D, et al (2021) A mathematical model for the quantification of a patient's sensitivity to checkpoint inhibitors and long-term tumour burden. Nature Biomedical Engineering 5(4):297–308. https://doi.org/10.1038/s41551-020-00662-0

Cao Y, Feng Y, Zhang Y, et al (2016) L-arginine supplementation inhibits the growth of breast cancer by enhancing innate and adaptive immune responses mediated by suppression of mdscs in vivo. BMC Cancer 16(1):1–11. https://doi.org/10.1186/s12885-016-2376-0

Chang AL, Miska J, Wainwright DA, et al (2016) CCL2 produced by the glioma microenvironment is essential for the recruitment of regulatory t cells and myeloid-derived suppressor cells CCL2 in treg and MDSC trafficking to glioma. Cancer research 76(19):5671–5682

Condamine T, Gabrilovich DI (2011) Molecular mechanisms regulating myeloid-derived suppressor cell differentiation and function. Trends in immunology 32(1):19–25

da Costa JMJ, Orlande HRB, da Silva WB (2018) Model selection and parameter estimation in tumor growth models using approximate bayesian computation-abc. Computational and Applied Mathematics 37(3):2795–2815. https://doi.org/10.1007/S40314-017-0479-0

Cukier R, Fortuin C, Shuler KE, et al (1973) Study of the sensitivity of coupled reaction systems to uncertainties in rate coefficients. i theory. Journal of Chemical Physics 59(8):3873–3878. https://doi.org/10.1063/1.1680571

Del Monte U (2009) Does the cell number 109 still really fit one gram of tumor tissue? Cell Cycle 8(3):505–506. https://doi.org/10.4161/cc.8.3.7608

Doblas S, He T, Saunders D, et al (2010) Glioma morphology and tumor-induced vascular alterations revealed in seven rodent glioma models by in

vivo magnetic resonance imaging and angiography. Journal of Magnetic Resonance Imaging 32(2):267–275. https://doi.org/10.1002/jmri.22263

Duraiswamy J, Kaluza KM, Freeman GJ, et al (2013) Dual blockade of PD-1 and CTLA-4 combined with tumor vaccine effectively restores T-cell rejection function in tumors. Cancer research 73(12):3591–3603

Eftimie R, Bramson JL, Earn DJ (2011) Interactions between the immune system and cancer: a brief review of non-spatial mathematical models. Bulletin of Mathematical Biology 73(1):2–32. https://doi.org/10.1007/s11538-010-9526-3

Fernandes C, Costa A, Osório L, et al (2017) Glioblastoma [Internet], Codon Publications, Brisbane, Australia, chap 11: Current standards of care in glioblastoma therapy, pp 197–241. https://doi.org/10.15586/codon.glioblastoma.2017.ch11

Flores-Toro JA, Luo D, Gopinath A, et al (2020) CCR2 inhibition reduces tumor myeloid cells and unmasks a checkpoint inhibitor effect to slow progression of resistant murine gliomas. Proceedings of the National Academy of Sciences 117(2):1129–1138. https://doi.org/10.1073/pnas.1910856117

Gabrilovich DI, Nagaraj S (2009) Myeloid-derived suppressor cells as regulators of the immune system. Nature Reviews Immunology 9(3):162–174. https://doi.org/10.1038/nri2506

Grover WH, Bryan AK, Diez-Silva M, et al (2011) Measuring single-cell density. Proceedings of the National Academy of Sciences 108(27):10,992–10,996. https://doi.org/10.1073/pnas.1104651108

Jafarnejad M, Gong C, Gabrielson E, et al (2019) A computational model of neoadjuvant PD-1 inhibition in non-small cell lung cancer. Journal of the American Association of Pharmaceutical Scientists 21(5):1–14. https://doi.org/10.1208/s12248-019-0350-x

Khajanchi S (2021) The impact of immunotherapy on a glioma immune interaction model. Chaos, Solitons & Fractals 152:111,346. https://doi.org/10.1016/j.chaos.2021.111346

Khajanchi S, Banerjee S (2017) Quantifying the role of immunotherapeutic drug T11 target structure in progression of malignant gliomas: Mathematical modeling and dynamical perspective. Mathematical Biosciences 289:69–77. https://doi.org/10.1016/j.mbs.2017.04.006

Khyat T, Jang SRJ (2022) On a discrete model of tumour–immune system interactions with blockade of immune checkpoints. Journal of Difference Equations and Applications 28(1):73–108. https://doi.org/10.1080/

10236198.2021.2023136

Kirschner D (2008) Uncertainty and sensitivity functions and implementation. http://malthus.micro.med.umich.edu/lab/usadata/

Kirschner D, Panetta JC (1998) Modeling immunotherapy of the tumor–immune interaction. Journal of Mathematical Biology 37(3):235–252. https://doi.org/10.1007/s002850050127

Kleponis J, Skelton R, Zheng L (2015) Fueling the engine and releasing the break: combinational therapy of cancer vaccines and immune checkpoint inhibitors. Cancer Biology & Medicine 12(3):201–208. https://doi.org/10.7497/j.issn.2095-3941.2015.0046

Korbecki J, Kojder K, Simińska D, et al (2020) CC chemokines in a tumor: a review of pro-cancer and anti-cancer properties of the ligands of receptors CCR1, CCR2, CCR3, and CCR4. International Journal of Molecular Sciences 21(21):8412. https://doi.org/10.3390/ijms21218412

Kuznetsov VA, Makalkin IA, Taylor MA, et al (1994) Nonlinear dynamics of immunogenic tumors: parameter estimation and global bifurcation analysis. Bulletin of Mathematical Biology 56(2):295–321. https://doi.org/10.1016/S0092-8240(05)80260-5

Lai X, Friedman A (2017) Combination therapy of cancer with cancer vaccine and immune checkpoint inhibitors: A mathematical model. PLoS One 12(5):e0178,479. https://doi.org/10.1371/journal.pone.0178479

Lai X, Stiff A, Duggan M, et al (2018) Modeling combination therapy for breast cancer with bet and immune checkpoint inhibitors. Proceedings of the National Academy of Sciences 115(21):5534–5539. https://doi.org/10.1073/pnas.1721559115

Liao KL, Bai XF, Friedman A (2014) Mathematical modeling of interleukin-35 promoting tumor growth and angiogenesis. PLoS One 9(10):e110,126. https://doi.org/10.1371/journal.pone.0110126

Liepe J, Kirk P, Filippi S, et al (2014) A framework for parameter estimation and model selection from experimental data in systems biology using approximate bayesian computation. Nature Protocols 9(2):439–456. https://doi.org/10.1038/nprot.2014.025

Lim M, Xia Y, Bettegowda C, et al (2018) Current state of immunotherapy for glioblastoma. Nature Reviews Clinical Oncology 15(7):422–442. https://doi.org/10.1038/s41571-018-0003-5

Mahlbacher GE, Reihmer KC, Frieboes HB (2019) Mathematical modeling of tumor-immune cell interactions. Journal of Theoretical Biology 469:47–60. https://doi.org/10.1016/j.jtbi.2019.03.002

Markowitz J, Wang J, Vangundy Z, et al (2017) Nitric oxide mediated inhibition of antigen presentation from DCs to CD4+ T cells in cancer and measurement of stat1 nitration. Scientific reports 7(1):1–13

Mirzaei N, Su S, Sofia D, et al (2021) A mathematical model of breast tumor progression based on immune infiltration. Journal of Personalized Medicine 11(10):1031. https://doi.org/10.3390/jpm11101031

Monu NR, Frey AB (2012) Myeloid-derived suppressor cells and anti-tumor t cells: a complex relationship. Immunological Investigations 41(6-7):595–613. https://doi.org/10.3109/08820139.2012.673191

Nikolopoulou E, Johnson L, Harris D, et al (2018) Tumour-immune dynamics with an immune checkpoint inhibitor. Letters in Biomathematics 5(2):S137–S159. https://doi.org/10.30707/LiB5.2Nikolopoulou

Nikolopoulou E, Eikenberry SE, Gevertz JL, et al (2021) Mathematical modeling of an immune checkpoint inhibitor and its synergy with an immunostimulant. Discrete & Continuous Dynamical Systems-B 26(4):2133

Ostrum Q, Gittleman H, Fulop J, et al (2015) Cbtrus statistical report: primary brain and central nervous system tumors diagnosed in the united states in 2008–2012. Neuro Oncology 17(Suppl 4):iv1–iv62. https://doi.org/10.1093/neuonc/nov189

Özköse F, Yılmaz S, Yavuz M, et al (2022) A fractional modeling of tumor–immune system interaction related to lung cancer with real data. European Physical Journal Plus 137(1):1–28. https://doi.org/10.1140/epjp/s13360-021-02254-6

Perlstein D, Shlagman O, Kogan Y, et al (2019) Personal response to immune checkpoint inhibitors of patients with advanced melanoma explained by a computational model of cellular immunity, tumor growth, and drug. PloS One 14(12):e0226,869. https://doi.org/10.1371/journal.pone.0226869

Pillay J, Den Braber I, Vrisekoop N, et al (2010) In vivo labeling with 2H2O reveals a human neutrophil lifespan of 5.4 days. Blood 116(4):625–627. https://doi.org/10.1182/blood-2010-01-259028

Postow MA, Chesney J, Pavlick AC, et al (2015) Nivolumab and ipilimumab versus ipilimumab in untreated melanoma. New England Journal of Medicine 372(21):2006–2017

Preusser M, Berghoff AS, Wick W, et al (2015a) Clinical neuropathology mini-review 6-2015: PD-L1: emerging biomarker in glioblastoma? Clinical Neuropathology 34(6):313. https://doi.org/10.5414/NP300922

Preusser M, Lim M, Hafler DA, et al (2015b) Prospects of immune checkpoint modulators in the treatment of glioblastoma. Nature Reviews Neurology 11(9):504–514. https://doi.org/10.1038/nrneurol.2015.139

Radunskaya A, Kim R, Woods II T (2018) Mathematical modeling of tumor immune interactions: a closer look at the role of a PD-L1 inhibitor in cancer immunotherapy. Spora: A Journal of Biomathematics 4(1):25–41. https://doi.org/10.30707/SPORA4.1Radunskaya

Reardon D, Omuro A, Brandes A, et al (2017) Os10. 3 randomized phase 3 study evaluating the efficacy and safety of nivolumab vs bevacizumab in patients with recurrent glioblastoma: Checkmate 143. Neuro Oncology 19(Suppl 3):iii21. https://doi.org/10.1093/neuonc/nox036.071

Ribeiro RM, Mohri H, Ho DD, et al (2002) In vivo dynamics of t cell activation, proliferation, and death in HIV-1 infection: why are CD4+ but not CD8+ T cells depleted? Proceedings of the National Academy of Sciences 99(24):15,572–15,577. https://doi.org/10.1073/pnas.242358099

Ros W, Delord J, Perets R, et al (2019) Efficacy and safety of pembrolizumab in previously treated advanced cervical cancer: results from the phase 2 keynote-158 study. Early Phase Clin Stud Novel Immunotherapeutics Oncol 37:117

Rutter EM, Stepien TL, Anderies BJ, et al (2017) Mathematical analysis of glioma growth in a murine model. Scientific Reports 7(2508):1–16. https://doi.org/10.1038/s41598-017-02462-0

Saio M, Radoja S, Marino M, et al (2001) Tumor-infiltrating macrophages induce apoptosis in activated CD8+ T cells by a mechanism requiring cell contact and mediated by both the cell-associated form of TNF and nitric oxide. The Journal of Immunology 167(10):5583–5593

Saltelli A, Tarantola S, Chan KS (1999) A quantitative model-independent method for global sensitivity analysis of model output. Technometrics 41(1):39–56. https://doi.org/10.1080/00401706.1999.10485594

Saltelli A, Ratto M, Andres T, et al (2008) Global sensitivity analysis: the primer. John Wiley & Sons Ltd, Chichester, England

Shariatpanahi SP, Shariatpanahi SP, Madjidzadeh K, et al (2018) Mathematical modeling of tumor-induced immunosuppression by myeloid-derived suppressor cells: Implications for therapeutic targeting strategies. Journal of

Theoretical Biology 442:1–10. https://doi.org/10.1016/j.jtbi.2018.01.006

Shi S, Huang J, Kuang Y (2021) Global dynamics in a tumor-immune model with an immune checkpoint inhibitor. Discrete & Continuous Dynamical Systems-B 26(2):1149–1170. https://doi.org/10.3934/dcdsb.2020157

Spagnuolo A, Gridelli C (2018) "Comparison of the toxicity profile of PD-1 versus PD-L1 inhibitors in non-small cell lung cancer": is there a substantial difference or not? Journal of Thoracic Disease 10(Suppl 33):S4065. https://doi.org/10.21037/jtd.2018.09.83

Srivastava MK, Zhu L, Harris-White M, et al (2012) Myeloid suppressor cell depletion augments antitumor activity in lung cancer. PloS One 7(7):e40,677. https://doi.org/10.1371/journal.pone.0040677

Stensjøen AL, Solheim O, Kvistad KA, et al (2015) Growth dynamics of untreated glioblastomas in vivo. Neuro Oncology 17(10):1402–1411. https://doi.org/10.1093/neuonc/nov029

Stepien TL, Lynch HE, Yancey SX, et al (2019) Using a continuum model to decipher the mechanics of embryonic tissue spreading from time-lapse image sequences: An approximate bayesian computation approach. PloS One 14(6):e0218,021. https://doi.org/10.1371/journal.pone.0218021

Stirling DR, Carpenter AE, Cimini BA (2021) Cellprofiler analyst 3.0: Accessible data exploration and machine learning for image analysis. Bioinformatics 37(21):3992–3994. https://doi.org/10.1093/bioinformatics/btab634

Storey KM, Lawler SE, Jackson TL (2020) Modeling oncolytic viral therapy, immune checkpoint inhibition, and the complex dynamics of innate and adaptive immunity in glioblastoma treatment. Frontiers in Physiology 11(151). https://doi.org/10.3389/fphys.2020.00151

Stupp R, Mason WP, Van Den Bent MJ, et al (2005) Radiotherapy plus concomitant and adjuvant temozolomide for glioblastoma. New England journal of medicine 352(10):987–996

Sunnåker M, Busetto AG, Numminen E, et al (2013) Approximate bayesian computation. PLoS Computational Biology 9(1):e1002,803. https://doi.org/10.1371/journal.pcbi.1002803

Takacs GP, Flores-Toro JA, Harrison JK (2021) Modulation of the chemokine/chemokine receptor axis as a novel approach for glioma therapy. Pharmacology & therapeutics 222:107,790

Takacs GP, Kreiger CJ, Luo D, et al (2022) Glioma-derived CCL2 and CCL7 mediate migration of immune suppressive CCR2+ myeloid cells into the

tumor microenvironment in a redundant manner. bioRxiv

Vetsika EK, Koukos A, Kotsakis A (2019) Myeloid-derived suppressor cells: major figures that shape the immunosuppressive and angiogenic network in cancer. Cells 8(12):1647

Xiao Y, Thomas L, Chaplain MA (2021) Calibrating models of cancer invasion: parameter estimation using approximate bayesian computation and gradient matching. Royal Society Open Science 8:202,237. https://doi.org/10.1098/rsos.202237

Yu JL, Jang SRJ (2019) A mathematical model of tumor-immune interactions with an immune checkpoint inhibitor. Applied Mathematics and Computation 362(C):1–11. https://doi.org/10.1016/j.amc.2019.06.037

Yu MW, Quail DF (2021) Immunotherapy for glioblastoma: Current progress and challenges. Frontiers in Immunology p 1637